The Ocean Boundary Layer beneath Larsen C Ice Shelf: Insights from Large-Eddy Simulations with a Near-Wall Model

CATHERINE A. VREUGDENHIL,[a,b] JOHN R. TAYLOR,[a] PETER E. D. DAVIS,[c] KEITH W. NICHOLLS,[c] PAUL R. HOLLAND,[c] AND ADRIAN JENKINS[d]

[a] *University of Cambridge, Cambridge, United Kingdom*
[b] *University of Melbourne, Melbourne, Victoria, Australia*
[c] *British Antarctic Survey, Cambridge, United Kingdom*
[d] *Northumbria University, Newcastle upon Tyne, United Kingdom*

(Manuscript received 1 August 2021, in final form 21 April 2022)

ABSTRACT: The melt rate of Antarctic ice shelves is of key importance for rising sea levels and future climate scenarios. Recent observations beneath Larsen C Ice Shelf revealed an ocean boundary layer that was highly turbulent and raised questions on the effect of these rich flow dynamics on the ocean heat transfer and the ice shelf melt rate. Directly motivated by the field observations, we have conducted large-eddy simulations (LES) to further examine the ocean boundary layer beneath Larsen C Ice Shelf. The LES was initialized with uniform temperature and salinity (T–S) and included a realistic tidal cycle and a small basal slope. A new parameterization based on previous work was applied at the top boundary to model near-wall turbulence and basal melting. The resulting vertical T–S profiles, melt rate, and friction velocity matched well with the Larsen C Ice Shelf observations. The instantaneous melt rate varied strongly with the tidal cycle, with faster flow increasing the turbulence and mixing of heat toward the ice base. An Ekman layer formed beneath the ice base and, due to the strong vertical shear of the current, Ekman rolls appeared in the mixed layer and stratified region (depth ≈ 20–60 m). In an additional high-resolution simulation (conducted with a smaller domain) the Ekman rolls were associated with increased turbulent kinetic energy, but a relatively small vertical heat flux. Our results will help with interpreting field observations and parameterizing the ocean-driven basal melting of ice shelves.

KEYWORDS: Ice shelves; Ocean dynamics; Turbulence; Mixing; Tides

1. Introduction

The melt rate of Antarctic ice shelves is expected to play a crucial role in determining global sea level rise in the future. Ice shelves are the floating extensions of ice sheets and act to buttress grounded ice (Schoof 2007). Thinning of ice shelves can destabilize the marine-based regions of the ice sheet, causing grounded ice flow to accelerate and thereby raising the sea level. In a changing climate, altered winds can enhance the flow of warm waters toward ice shelves, for example, in the Weddell Sea (Hellmer et al. 2012; Darelius et al. 2016) and Amundsen Sea (Jenkins et al. 2018; Holland et al. 2019). Warming the waters beneath Antarctic ice shelves will enhance their basal melting (Shepherd et al. 2004; Pritchard et al. 2012; Paolo et al. 2015). However, the turbulent ice shelf–ocean boundary layer mechanisms that physically transport heat toward the ice base are not well constrained and remain a source of major uncertainty in predicting future sea level (Dinniman et al. 2016). Here, we use large-eddy simulations (LES) of the ocean beneath an ice shelf to examine the influence of turbulence and stratification on the melt rate.

Observations of the basal melting of Antarctic ice shelves have traditionally been sparse due to the difficulty in observing these regions. Recently, borehole observations taken at Larsen C Ice Shelf (Fig. 1, left) provided a glimpse of the rich dynamics in the underlying ocean (Nicholls et al. 2012; Davis and Nicholls 2019, hereafter DN19). These measurements took place over more than a year and were the first extended observations of small-scale turbulence beneath an ice shelf. Turbulence instrument clusters placed at depths of 2.5 and 13.5 m showed strong turbulence consistent with a logarithmic "law-of-the-wall" boundary layer (e.g., Pope 2000). The observations also revealed a spring–neap tidal signal superimposed on a weaker background flow, with the level of turbulence closely tied to the tidal cycle. CTD (conductivity–temperature–depth) profiles showed a cold and salty ocean with a well-mixed layer beneath the ice base (to ~50-m depth) followed by weak stratification in both salinity and temperature (to ~80-m depth) and a uniform temperature and salinity far-field ocean below. A year-averaged basal melt rate of 0.7 m yr^{-1} was measured using upward-looking sonar. The Larsen C Ice Shelf borehole measurements provided evidence that the water flowing into the sub-ice cavity (from the southeast) was cold High Salinity Shelf Water, rather than the relatively warmer Modified Warm Deep Water observed outside the cavity in ship-based measurements (Nicholls et al. 2012; Bathmann et al. 1994; Nicholls et al. 2004).

Since the borehole observations sampled a fixed position beneath the ice shelf, it was not clear to what extent the local stratification reflects a local balance between melting and vertical mixing, or whether upstream advection plays a significant role. This distinction is important when developing parameterizations for turbulence in the ice shelf–ocean boundary layer and for planning observational campaigns. Here, we use LES closely based on the observations from DN19 to study

Corresponding author: Catherine A. Vreugdenhil, cat.vreugdenhil@unimelb.edu.au

DOI: 10.1175/JPO-D-21-0166.1

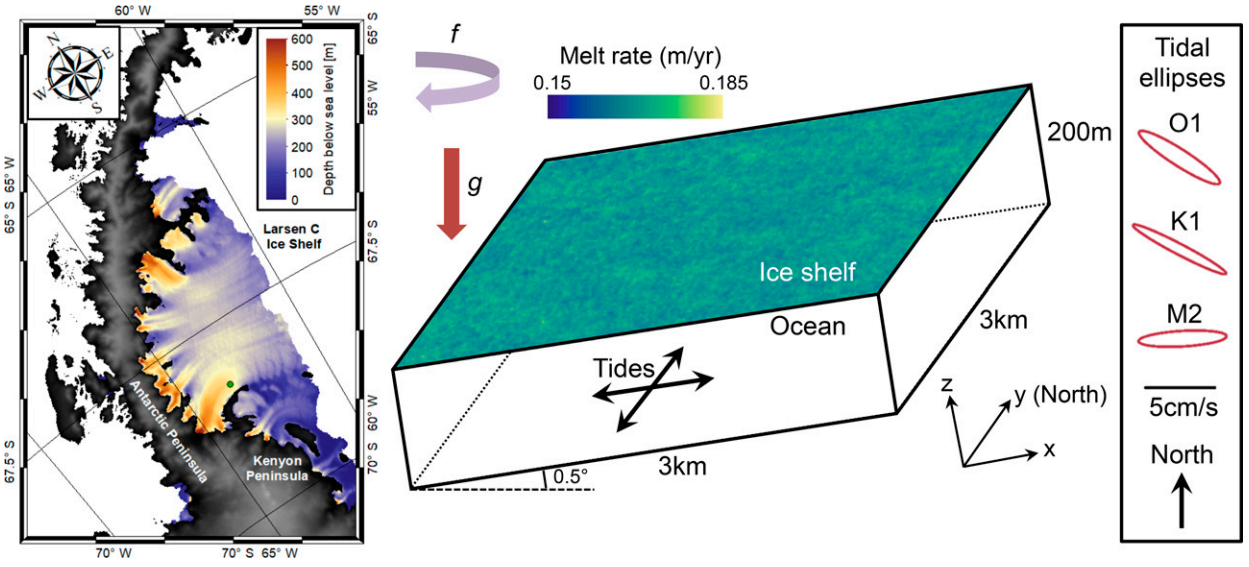

FIG. 1. Schematic showing the simulations of the ocean beneath the melting Larsen C Ice Shelf. (left) Map of Larsen C Ice Shelf with hot water drill access hole shown as green dot. The color contours show the ice base depth below sea level from Bedmap2 (Fretwell et al. 2013). (center) Simulated rectangular domain (not to scale) that is tilted in the x direction to model the slope of the ice shelf base. The melt rate is a snapshot taken at day 70 of the large domain simulation. (right) Tidal ellipses that match the three strongest modes from the observations (DN19).

locally (by this we mean a purely vertical balance) generated turbulence and stratification beneath Larsen C Ice Shelf. However, it is important to note that, even if the stratification can be explained by a local balance, there is no guarantee that this solution is unique. It is possible that the same T–S profiles could also be obtained through nonlocal processes.

Recent years have also seen other observational campaigns begin to characterize the ocean boundary layer beneath different Antarctic ice shelves. For example, indirect measurements of flow in the cold ocean cavity beneath Ronne Ice Shelf imply strong turbulence, weak stratification, and relatively low melt rates (Jenkins et al. 2010). These features are in common with observations of Fimbul Ice Shelf (Hattermann et al. 2012) and regions of Ross Ice Shelf (Arzeno et al. 2014). Other borehole observations with turbulence measurements have revealed more strongly stratified regions and evidence of double diffusion beneath George VI Ice Shelf (Kimura et al. 2015) and near the grounding line of Ross Ice Shelf (Begeman et al. 2018). Pine Island Glacier Ice Shelf also has regions of very strong stratification in the underlying ocean, as revealed by an autonomous underwater vehicle (Stanton et al. 2013; Kimura et al. 2016). Our LES will have implications for sub-ice shelf circulations similar to that beneath Larsen C Ice Shelf and will help to explain some of the differences between sub-ice shelf circulations around Antarctica.

The physical processes involved in the melting of ice shelves, including turbulent mixing of heat and salt toward the ice, typically require parameterization in ocean models because they occur on length scales far smaller than the model resolution. The three-equation model is a common melt parameterization used in coarser ocean models or with observations further from the ice (McPhee et al. 1987; Jenkins 1991; Holland and Jenkins 1999; Malyarenko et al. 2020). This model is based on the conservation of heat [Eq. (1)] and salt [Eq. (2)], along with an equation for the freezing point of water [Eq. (3)],

$$c_w \rho_w C_d^{1/2} U \Gamma_T (T - T_b) = \rho_i L_i m, \tag{1}$$

$$\rho_w C_d^{1/2} U \Gamma_S (S - S_b) = \rho_i S_b m, \tag{2}$$

$$T_b = \lambda_1 S_b + \lambda_2 + \lambda_3 P. \tag{3}$$

Heat conduction into the ice has been neglected, which is a condition regularly used with the assumption that the conducted heat flux is small compared to the latent heat flux (Holland and Jenkins 1999). Inputs into the above formulation are the flow speed U, temperature T, and salinity S, which are evaluated at a specific depth. Outputs are the temperature T_b and salinity S_b at the boundary and the melt rate m. However, choices still need to be made in setting realistic drag coefficients C_d and heat Γ_T and salt Γ_S transfer coefficients. Other constants are the specific heat capacity of water c_w, the latent heat of fusion L_i, reference densities of ice ρ_i and water ρ_w, pressure P, and coefficients in a linearized expression for the freezing point of seawater, λ_1, λ_2, and λ_3 (Jenkins 2011). Drag and transfer coefficients can be chosen to reproduce observed time-averaged melt rates, for example the three-equation model does a reasonable job of predicting melt rates for Larsen C Ice Shelf (DN19) and Ronne Ice Shelf (Jenkins et al. 2010). The three-equation model does less well when applied to sites with stronger stratification and double diffusion (Kimura et al. 2015; Begeman et al. 2018). It is crucial to have accurate melt parameterizations to model future climate

scenarios, but to achieve this we need to first understand the processes determining the ice shelf melt rate.

There are many physical processes influencing the ocean beneath ice shelves, several of which have been examined using idealized laboratory or numerical models. These include the meltwater plume for a vertical (Gayen et al. 2016; McConnochie and Kerr 2016) or sloped (McConnochie and Kerr 2018; Mondal et al. 2019) ice face, double diffusion (Martin and Kauffman 1977; Keitzl et al. 2016; Middleton et al. 2021; Rosevear et al. 2021), and stratification (Vreugdenhil and Taylor 2019). A one-dimensional model of the ocean beneath a melting ice shelf, which included Earth's rotation, stratification, and a meltwater plume, revealed the impact of an Ekman layer and strong across-slope flow (Jenkins 2016, 2021). By necessity, turbulent mixing was parameterized in this one-dimensional model, but we might anticipate three-dimensional turbulent structures to emerge in the ice shelf–ocean boundary layer. For example, Deusebio et al. (2014) observed Ekman rolls in numerical simulations of a weakly stratified Ekman layer. These structures are the nonlinear manifestation of linear instabilities of an Ekman spiral, where the turning of the horizontal velocity with depth creates an inflection point in the speed profile that can become unstable (Lilly 1966; Faller and Kaylor 1966; Brown 1972).

The defining feature of LES is explicitly resolving the most energetic three-dimensional turbulence, while parameterizing only the smaller motions with a subgrid-scale (SGS) model. Here, LES is used to study the combined effects of Earth's rotation, tides, and turbulence beneath a weakly sloped ice base under conditions consistent with Larsen C Ice Shelf observations reported in DN19. Our approach was to isolate a few key physical processes present in the observations (e.g., realistic tidal forcing, dynamic melting), while excluding processes whose presence was inconclusive in the observations (e.g., large-scale horizontal temperature/salinity gradients, double diffusion). Comparing the LES results to the observations shows the relative importance of the processes that are captured and those that are missing. By reducing the model physics, we also learn about the fluid dynamics that might be obscured by including additional physical processes. A newly derived near-wall model parameterized turbulence near the ice base, as outlined in section 2. The LES are compared with Larsen C Ice Shelf observations in section 3. The results provide new insight into the bulk properties of the boundary layer, the formation of Ekman rolls and the transport of heat toward the ice base by boundary layer turbulence. In section 4, the results are discussed further in the context of the surrounding ocean dynamics, paving the way for future observational and modeling studies. Conclusions are in section 5.

2. Model design

The ocean beneath a melting ice shelf was modeled using idealized large-eddy simulations (Fig. 1). The initial and boundary conditions, along with other relevant simulation parameters (details in section 2a), closely followed field observations from December 2011 to January 2013 in the southern region of Larsen C Ice Shelf. Nicholls et al. (2012) and DN19 include full details of the observations. The model domain was tilted such that the top boundary was aligned with the sloping ice base. There were periodic boundary conditions in the two directions parallel to the ice base. A near-wall parameterization was applied as a boundary condition at the top of the domain, which resulted in a spatially and temporally varying basal melt rate (details in section 2b). The lower boundary condition was impenetrable and free-slip, with no-flux conditions for temperature and salinity.

Tidal forcing was applied through a pressure gradient to match the three strongest observed tidal constituents (O_1, K_1, and M_2) that resulted in a strong spring–neap cycle. The rectangular model domain was sloped away from the horizontal by 0.5° to match the weak slope at the observational site (based on Bedmap2; Fretwell et al. 2013). While the strong tides were hypothesized to set the flow, the slope was matched to allow for the possibility of a meltwater plume. The Coriolis acceleration was included in the slope-parallel momentum equations using the traditional approximation.

The simulation shown in Fig. 1 had a domain of 3 km × 3 km × 200 m with 480 × 480 × 101 uniform grid points. The simulation was initialized with uniform temperature T and salinity S to match the far-field values from the Larsen C Ice Shelf observations. The initial slope-parallel velocities are set to the velocities expected from the tidal forcing. Importantly, the initial T, S, and velocity were spatially constant (aside from some small amplitude random noise). By comparing the subsequent model T–S profiles with the observations, we were able to test whether the observed bulk boundary layer properties could be reproduced by the local turbulence and melting. This setup in the relatively large domain allowed study of the turbulence evolution over several spring–neap cycles in simulations lasting for over 100 days. To study the influence of model resolution and the role of small-scale turbulence, another simulation was conducted in a smaller domain 600 m × 200 m × 200 m with 384 × 128 × 401 uniform grid points. This domain was designed to be orientated roughly along the tidal ellipses of the diurnal tides, O_1 and K_1 (more details in section 3c).

The entire evolution of the simulations was of interest, but we particularly focused on the interval where the vertical gradient of the temperature and salinity profiles most closely matched the observations. This was to ensure that the depths of the mixed layer and the stratified region were similar in the simulations and observations. The simulations were an initial value problem as there was no source of restoring heat and salinity, meaning that the boundary layer continued to freshen and cool and there was no long-term equilibrated state. Of course, it is unlikely that the small-scale flow under a melting ice shelf is in an unchanging equilibrated state either (e.g., synoptic and seasonal variability is expected). It is worth noting that the simulations do not attempt to include any large-scale horizontal gradients in T, S that may be of importance in maintaining steady-state conditions (Jenkins 2016, 2021). The remainder of this section outlines further details of the numerical simulations.

a. *Numerical simulation setup*

The simulations solved the incompressible Navier–Stokes momentum equation (with the Boussinesq approximation), the conservation of mass, heat, and salt and a linear equation of state,

$$\frac{D\mathbf{u}}{Dt} = -\frac{1}{\rho_0}\nabla p + \nu\nabla^2\mathbf{u} + \mathbf{F} - \frac{\Delta\rho}{\rho_0}g(\sin\theta\mathbf{i} + \cos\theta\mathbf{k}) - f\mathbf{k}\times\mathbf{u} - \nabla\cdot\boldsymbol{\tau}, \quad (4)$$

$$\nabla\cdot\mathbf{u} = 0, \quad \frac{DT}{Dt} = \kappa_T\nabla^2 T - \nabla\cdot\boldsymbol{\lambda}_T, \quad \frac{DS}{Dt} = \kappa_S\nabla^2 S - \nabla\cdot\boldsymbol{\lambda}_S, \quad (5)$$

$$\frac{\Delta\rho}{\rho_0} = -\alpha(T - T_0) + \beta(S - S_0). \quad (6)$$

where $\mathbf{u} = (u, v, w)$ was the velocity vector; (x, y, z) was the position vector; $\mathbf{i}$ and $\mathbf{k}$ were the unit vectors in the x and z directions, respectively; t was time; p was pressure; T was temperature; S was salinity; and ρ was density. The ice base slope was specified in the x direction. The reference values of temperature, salinity, and density were T_0, S_0, and ρ_0, respectively, and $\Delta\rho = \rho - \rho_0$. The gravitational acceleration was $g = 9.81\ \mathrm{m\ s^{-2}}$ and the slope away from the horizontal was $\theta = 0.5°$. The coefficients of thermal expansion and saline contraction were $\alpha = 3.28\times10^{-5}\ °\mathrm{C^{-1}}$ and $\beta = 7.84\times10^{-4}\ \mathrm{psu^{-1}}$, respectively, which were chosen to be consistent with the ocean state beneath Larsen C Ice Shelf (Gibbs Seawater Oceanographic Toolbox; McDougall and Barker 2011). We used realistic values of the molecular viscosity $\nu = 1.8\times10^{-6}\ \mathrm{m^2\ s^{-1}}$ and the molecular diffusivity of heat $\kappa_T = 1.3\times10^{-7}\ \mathrm{m^2\ s^{-1}}$ (Prandtl number $\mathrm{Pr} = \nu/\kappa_T = 13.8$) and salt $\kappa_S = 7.4\times10^{-10}\ \mathrm{m^2\ s^{-1}}$ (Schmidt number $\mathrm{Sc} = \nu/\kappa_S = 2432$). The Coriolis parameter was $f = -1.35\times10^{-4}\ \mathrm{rad\ s^{-1}}$. The tidal forcing $\mathbf{F} = (F_x\mathbf{i} + F_y\mathbf{j})$ includes the three dominant tidal constituents (O_1, K_1, and M_2). As described in appendix A, the form of $\mathbf{F}$ was set so that the far-field in the model velocity matched the tidal ellipse and phase for each of the three constituents in the observations beneath Larsen C reported in DN19.

The subgrid-scale contributions to the momentum $\boldsymbol{\tau}$, heat $\boldsymbol{\lambda}_T$, and salt $\boldsymbol{\lambda}_S$ equations were calculated using the anisotropic minimum dissipation (AMD) model (Rozema et al. 2015; Abkar and Moin 2017; Verstappen 2016). This subgrid-scale model was expected to work especially well in the present simulations, which were strongly turbulent with relatively weak stratification (Vreugdenhil and Taylor 2018). The AMD model was setup in the same manner as past simulations of under-ice shelf flow by Vreugdenhil and Taylor (2019).

Equations (4)–(6) were discretized into Fourier modes in the periodic slope-parallel directions and with second-order finite differences in the wall-bounded vertical direction (see Taylor 2008). When moving from Fourier space to physical space, a 2/3 dealiasing rule was applied (Orszag 1971). The equations were solved with a low-storage third-order Runge–Kutta method and a semi-implicit Crank–Nicholson method was used for the viscous and diffusive terms. The Courant–Friedrichs–Lewy condition was used for the adaptive time step.

b. Near-wall model algorithm

The LES resolution was too low to resolve turbulence close to the ice–ocean boundary where the distance from the boundary limits the size of turbulent eddies. Instead, a near-wall model was implemented to estimate the basal stress, melt rate, and heat and salt fluxes given the temperature, salinity, and velocity at the top grid point of the computational domain. Details of the near-wall model are in appendix B, with key features described here.

The location of the uppermost computational grid point was placed in the law-of-the-wall logarithmic layer where Monin–Obukhov scaling was expected to hold (Vreugdenhil and Taylor 2019). Observations beneath Larsen C Ice Shelf suggested that the logarithmic layer extended to at least 2.5 m in depth (DN19). In our LES, the first grid point was placed at 1 m in the large domain case and 0.25 m in the small domain case. A smooth ice base formulation was chosen as the roughness inferred from DN19 was small. The near-wall model used Monin–Obukhov scaling coupled with the diffusive melt equations (McPhee et al. 1987; Holland and Jenkins 1999) to solve for the fluxes of heat, salt, and momentum at the ice base. The near-wall model was verified against past LES of the logarithmic layer that resolved the viscous sublayer (resolved LES from Vreugdenhil and Taylor 2019). The near-wall model is expected to work well for the strongly turbulent and weakly stratified ocean beneath Larsen C Ice Shelf. If stratification dominates the flow, as may be the case beneath George VI Ice Shelf, for example (Kimura et al. 2015), the near-wall model may not be appropriate. The melt rate from the near-wall model was updated each time step and had spatial dependence, as shown in Fig. 1 for the Larsen C Ice Shelf simulation.

Compared to the three-equation model [Eqs. (1)–(3)], the advantage of the near-wall model algorithm is that it does not assume constant values of the drag, heat, and salt transfer coefficients (C_d, Γ_T, and Γ_S). For an under-ice flow whose turbulence level does not vary significantly (zero or very weak stabilizing stratification) the three-equation model will do a reasonable job of modeling the flow, provided that the correct values of C_d, Γ_T, and Γ_S are chosen. Note that, even without stabilizing stratification, if the turbulence level varies significantly then a varying drag coefficient may be required to accurately model the flow at different times [see fundamental turbulence review in Pope (2000)]. Beneath Larsen C Ice Shelf there were large fluctuations in the ocean turbulence due to the tides, with the additional complication of stabilizing stratification due to melting (DN19). From the outset it was unclear how turbulence and stratification would interact during the tidal cycle and impact the melt rate, which could have feedback effects on the water column stratification and turbulence itself. Here we avoided making assumptions about C_d, Γ_T, and Γ_S but rather calculated them using the near-wall model algorithm.

3. Results

a. Bulk properties of the flow

The simulated flow beneath Larsen C Ice Shelf was initialized with uniform temperature, salinity, and tidal velocities. The strong tidal forcing followed a spring–neap cycle that

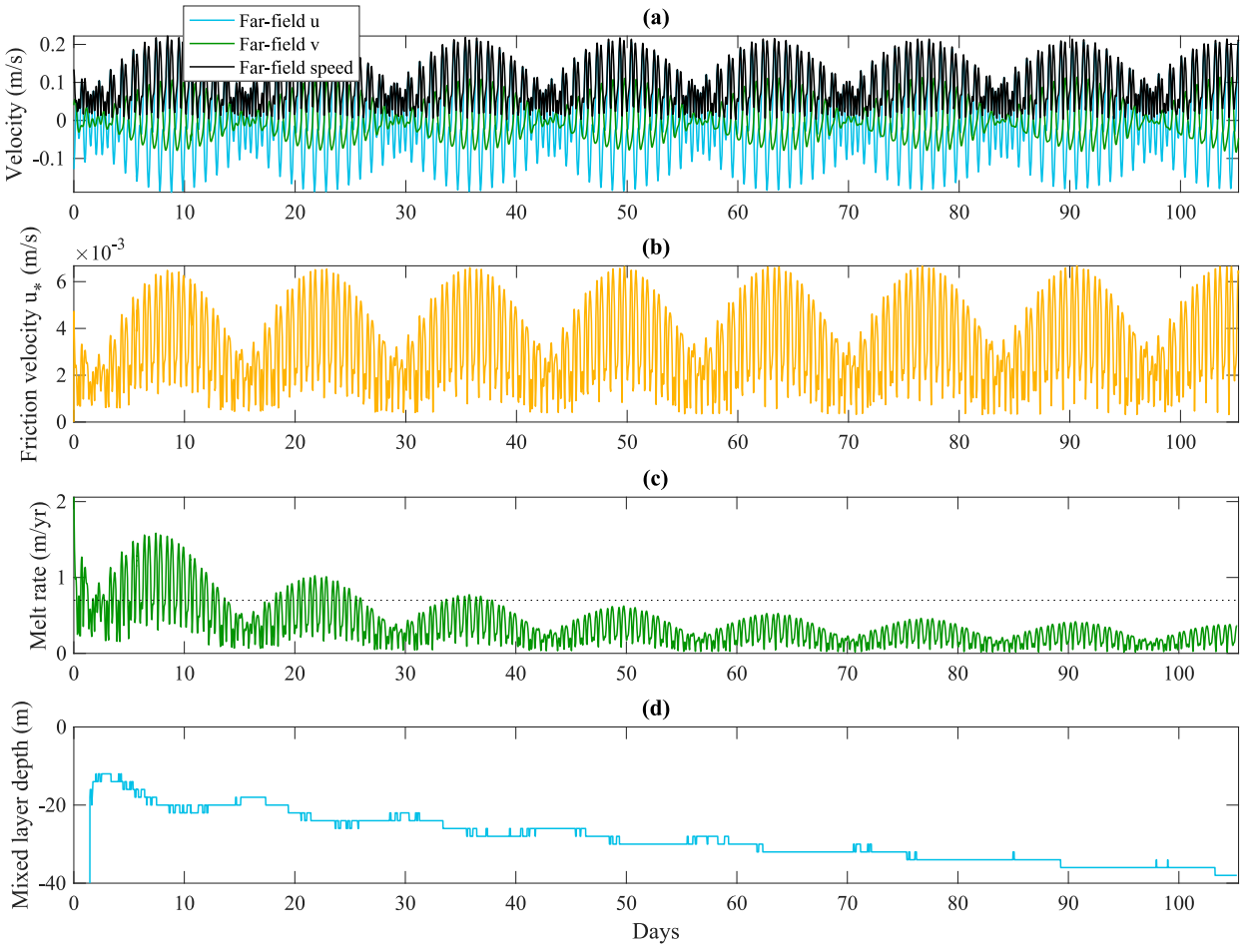

FIG. 2. Time dependence of (a) far-field slope-parallel velocities and speed, (b) friction velocity calculated at the ice base [u_*, Eq. (7)], (c) ice shelf melt rate, and (d) the mixed layer depth for the large domain simulation. All results have been averaged in the slope-parallel directions across the domain. In (c) the dotted line shows the year-averaged observed melt rate (DN19). The jumps in mixed layer depth are set by model resolution.

appears clearly in the bulk velocities (Fig. 2a). The tidal cycle was also a key factor setting the friction velocity,

$$u_* = \sqrt{\tau/\rho_0}, \tag{7}$$

which is a measure of the strength of the stress τ at the ice base. As shown in Fig. 2b, faster tidal velocities resulted in a larger stress at the ice base and hence a larger friction velocity. Strong turbulence during spring phases of the tidal cycle mixed heat toward the ice base, enhancing the melt rate (Fig. 2c). The melting ice base freshened and cooled the upper water column, creating a mixed layer that deepened throughout the simulation (Fig. 2d). The mixed layer depth was measured as the depth at which the density was equal to $\rho_{\text{top}} + 0.01\ \text{kg m}^{-3}$. To put this in context, the top-to-bottom density difference was $0.04\ \text{kg m}^{-3}$ (at day 70). Since the melt rate was dependent on the temperature and salinity in the near-ice region, and since there were periodic boundary conditions in the directions parallel to the ice base, over time the melt rate slowly decreased as the mixed layer became fresher and colder. The melt rate from field observations ($0.7\ \text{m yr}^{-1}$) is consistent with the initial melt rate diagnosed in the LES.

The deepening mixed layer is also shown in the evolving temperature and salinity profiles (Figs. 3a,b). Despite initializing the model with uniform T and S, the profiles around day 70 compare reasonably well with the observed CTD profiles, in particular when considering the vertical gradient profiles (Figs. 3c,d). It is worth noting that the model is colder and fresher in the mixed layer at the times when the gradient profiles most closely match. Nevertheless, the overall shape of the profiles is similar to observations with a well-mixed region immediately beneath the ice base, followed by stratification, and then the far-field region as yet unaffected by the local melting ice. This shows that the basic vertical structure in the CTD profiles can be generated through local production of meltwater and vertical mixing.

On the T–S diagram (Fig. 3e), the initial uniform T, S are represented by a single point at $T = -1.955$°C and $S = 34.57$ psu. As time progressed, the upper water column freshened and cooled and the profiles extended toward the T–S freezing point

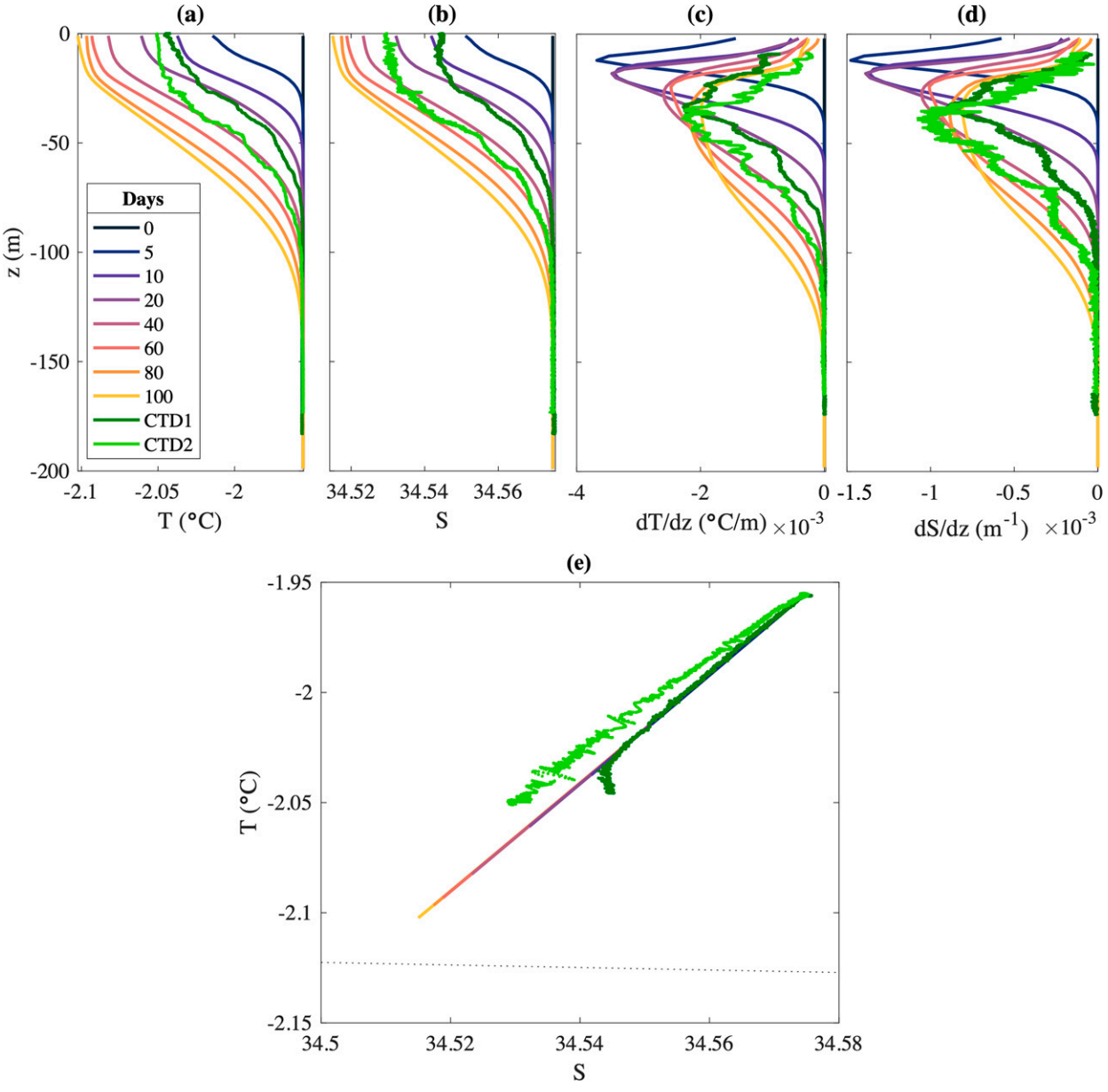

FIG. 3. Vertical profiles of (a) temperature and (b) salinity, vertical gradients of (c) temperature and (d) salinity, and (e) the T–S diagram. The simulation profiles are shown at different points in time and have been averaged in the slope-parallel directions across the domain. Note that the topmost values of T, S are from the top of the water column (the first grid cell beneath the ice) rather than being the ice–ocean boundary conditions T_b, S_b. Observations from Larsen C Ice Shelf are also shown where CTD1 (dark green) was taken 7 h before CTD2 (light green) (Nicholls et al. 2012; DN19). The observed profiles were smoothed using a moving average filter prior to the gradient being calculated for (c) and (d), where the top and bottom 5% of the vertical gradient profiles are not shown as they are outside the window of the moving average filter. In (e) the freezing point at the pressure of the ice base is shown as the dotted line.

line (dotted line on Fig. 3e). The T–S slope is consistent with the first set of CTD observations (dark green), except near the ice base where the observed profile diverged, possibly due to brine rejection from refreezing near the hot-water drilled borehole. The latter set of CTD observations (light green) was only taken 7 h later but shows a shift in T–S angle which was not seen in the LES. This is a clear indication of lateral advection across the observation site, where the advected waters could be influenced by ice melting into a different "source water," something the model cannot be expected to capture because of the periodic boundary conditions.

To compare with the DN19 observations, the covariance method was used to estimate the friction velocity by using Reynolds stresses at different depths,

$$u_*^{\text{covar}} = [(u'w')^2 + (v'w')^2]^{1/4}, \tag{8}$$

where the LES u_*^{covar} included both the resolved and subgrid-scale contributions. The dash indicates deviation from the mean, where the LES used the slope-parallel mean and the observations used the burst-averaged time mean (the observations were taken for 15-min bursts every 2 h). In Fig. 4a the friction velocity calculated using the covariance method [Eq. (8)] from the LES is compared with the DN19 observations. The chosen depths, 2.5 and 13.5 m, corresponded to the two velocity instruments in the field observations referred to as the upper and lower modular acoustic velocity sensor (MAVS), respectively. To put this in perspective, the depth of the Ekman layer (which was set up within the first 12-h period) was roughly $\sqrt{2\nu_{\text{SGS}}/f} = 3.8\,\text{m}$, where $\nu_{\text{SGS}} \approx 10^{-3}\ \text{m}^2\ \text{s}^{-1}$ was the maximum turbulent viscosity. While the LES has generally smaller covariance friction velocities, the trend was the same as the DN19 observations with the Upper MAVS having a stronger friction velocity than the Lower MAVS. The smaller friction velocities in the LES might be due to smooth ice assumed in the near-wall model, but could also be due to turbulence from other sources that were not present in the idealized simulations (further discussion in section 4).

The drag coefficient, $C_d^{\text{covar}} = (u_*^{\text{covar}}/U)^2$, increased at low flow speeds in both the LES and Upper MAVS observations as shown in Fig. 4b. For the Upper MAVS, DN19 attributed this to the instrument moving into and out of the logarithmic layer. A different explanation emerges after considering the LES evolution in Fig. 4c. The tidal current (gray dashed line) drove the main flow, with the friction velocity at the ice base (orange line) following closely. The shear turbulence generated at the ice base then took time to propagate to depth, resulting in an offset for u_*^{covar} measured at depth as shown for day 76 in Fig. 4d. The tidal current with depth is also included for day 76 in Fig. 4e. One reason for the time offset is that the weak stratification in the mixed layer needed to be eroded away by the turbulence as it propagated to depth, as shown for day 76 in Fig. 4f. Thus when the current speed U dropped toward zero, there was still turbulence at depth so u_*^{covar} was still large, and C_d^{covar} increased. By the time the turbulence and u_*^{covar} started to decrease, the current speed had increased again, and C_d^{covar} decreased. This explains the increase in C_d^{covar} at small current speeds when C_d^{covar} was calculated using the current speed far from the ice base. This explanation is also consistent with the hysteresis shown in Figs. 4a and 4b. Overall, the u_*^{covar} at depth were smaller than u_* calculated at the ice base as shown in Fig. 4c. The u_*^{covar} also decreased further from the ice base, as less turbulence managed to propagate to these depths.

The ice base melt rate is strongly tied to the current speed as shown in Fig. 5a. The chosen depths for the current speed comparison were 2.5 and 13.5 m (corresponding to the MAVS) along with a notional far-field depth at 190 m. For faster current speeds there was more turbulence near the ice, larger friction velocity u_* (Fig. 5b), and hence more melting. However, the melt rate and u_* are not unique functions of the far-field speed (cyan symbols) but exhibited an asymmetric response to the tidal cycle, where the period of each loop corresponds to a single M_2 tidal cycle. These (cyan) loops are also slightly offset compared to the upper water column results (red and blue lines). This offset can be explained by the presence of a buoyant meltwater plume. The meltwater was relatively less dense and formed an upslope buoyant plume that ended up being diverted to mainly across slope movement due to geostrophy (Jenkins 2016). Evidence for the meltwater plume is most clearly shown by comparing flow velocities between simulations with and without the ice base slope (Fig. C1 in appendix C). The meltwater plume has some velocity in the upper region, which led to an offset in the response of the melt rate and u_* to changes in the far-field current (cf. Fig. 5a with Fig. C2 in appendix C). When the buoyant current is in the same direction as the tidal current, the current speed and melt rate are enhanced, and when they are in opposite directions the current speed and melt rate are suppressed.

The LES can help to determine whether setting single constant values of the transfer coefficients in the three-equation model is appropriate. The heat and salt transfer coefficients in Figs. 5d and 5e were calculated as

$$\Gamma_T = \frac{\kappa_T \left|\frac{\partial T}{\partial z}\right|_b}{u_*(T - T_b)}, \quad \Gamma_S = \frac{\kappa_S \left|\frac{\partial S}{\partial z}\right|_b}{u_*(S - S_b)}, \tag{9}$$

where $|\partial T/\partial z|_b$ and $|\partial S/\partial z|_b$ are, respectively, the diffusive heat and salt fluxes across the ice–ocean boundary. For different depths, the only parameters in Eq. (9) that changed were T and S and the remaining values were obtained from the near-wall model [Eqs. (9) are rewritten from Eqs. (B14) in appendix B]. The mixed layer gave Γ_T, Γ_S similar to those inferred from observations beneath Ronne Ice Shelf of $\Gamma_T = 0.011$ and $\Gamma_S = 3.1 \times 10^{-4}$ (Jenkins et al. 2010). When comparing the results from the upper mixed layer to the far-field, the depth dependence of Γ_T is particularly strong. Transfer coefficients for the three-equation model did not vary significantly when the chosen depth of input values was within the top 15 m of the mixed layer, but the concept of depth-independent transfer coefficients fails when applied to the far-field values below the pycnocline. This result was not surprising as the three-equation model was formulated to work with values up to the outer edge of the boundary layer. The three-equation model was not designed to parameterize mixing through the pycnocline and, from the simulations shown here, we caution that it should not be used beyond the boundary layer (in this case the mixed layer).

In Fig. 5c, the drag coefficient using friction velocity calculated at the ice base, $C_d = (u_*/U)^2$, is plotted against speed at the three depths. The drag coefficient calculated with the ice base friction velocity C_d did not vary much with flow speed at 2.5-m depth, with more variance at 13.5-m depth and in the far field. This is also demonstrated in the vertical profiles of C_d in Fig. 5f. The LES shows that the drag coefficient was a quite well defined quantity within the mixed layer, as long as the interfacial stress is used. In contrast, the covariance drag coefficient C_d^{covar} (Fig. 4b) does not tend as nicely to a single value, especially if the measurement was made further from the ice base. In other words, the interfacial stress is not well represented by the covariance-calculated stress, especially far

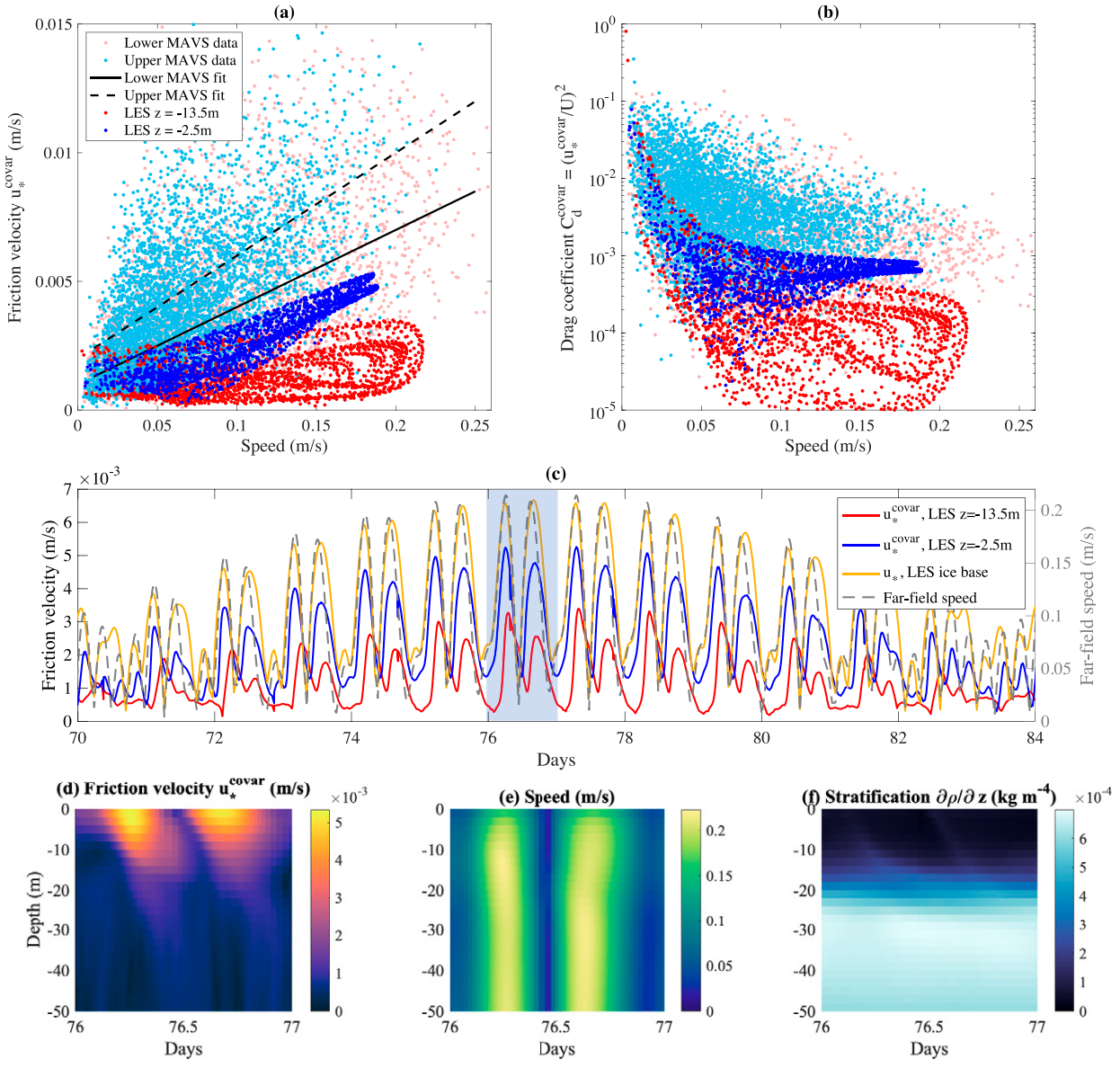

FIG. 4. (a) Friction velocity and (b) drag coefficient against current speed, where u_*^{covar} was calculated using the covariance method [Eq. (8)]. Symbol and line color corresponds to the depth at which u_*^{covar}, C_d^{covar}, and current speed were calculated (blue = 2.5-m depth, red = 13.5-m depth). In the LES, all variables were averaged in the slope-parallel directions and the results are shown for days 70–100 only. Also included are the DN19 observations over more than a year period for the upper MAVS (2.5-m depth, light blue) and lower MAVS (13.5-m depth, light pink) and the best fits to the observed data (black lines). (c) The evolution of the LES u_*^{covar}, along with u_* calculated at the ice base [Eq. (7); orange line] and the far-field speed (dashed gray). The evolution of LES (d) u_*^{covar}, (e) speed, and (f) stratification in the uppermost 50 m of the domain for day 76 [shaded region in (c)].

from the ice (13.5 m or deeper). This is because, fundamentally, it is not a constant stress boundary layer.

Observations are unable to make any direct measurement of the shear stress at the ice/ocean interface. Even borehole observations like DN19 are limited to estimating the shear stress from measurements a few meters from the ice base. Instead the basal stress is commonly inferred by assuming that the measured velocity some distance from the ice is related to the friction velocity through a constant drag coefficient. Our LES show that it might be acceptable to use a constant value of C_d in models that resolve the mixed layer, although the drag coefficient does vary (by up to an order of magnitude) at very low flow speeds.

b. *Ekman rolls*

The simulated flow had significant structure at scales from 100 m to 1 km in the ice slope-parallel directions, despite the fact that the computational domain was homogeneous in

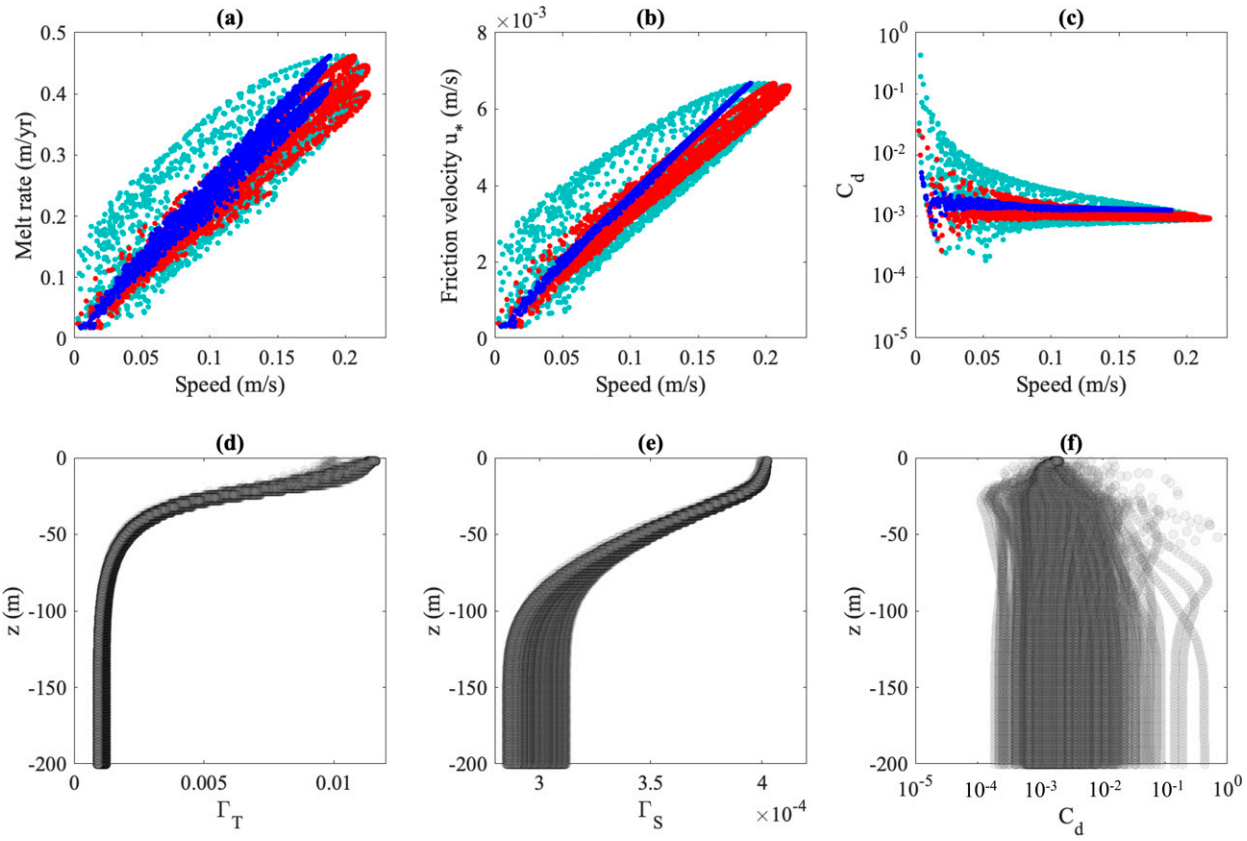

FIG. 5. The (a) melt rate, (b) friction velocity, and (c) drag coefficient against speed. The transfer coefficients for (d) heat and (e) salt, and (f) the drag coefficient with depth. The current speed and melt rate were averaged in the slope-parallel directions across the domain. The results are shown for days 70–100 of the simulation only. In (a)–(c) the symbol color corresponds to the depth at which C_d and the current speed were calculated (blue = 2.5-m depth, red = 13.5-m depth, and cyan = far field at 190-m depth). In (c) and (f) the drag coefficient was calculated using friction velocity at the ice base [Eq. (7)].

these directions. Figure 6 shows elongated features in the slope-parallel speed at 20-m depth, with associated upward and downward motions. A signature of these features also appears in temperature and salinity as undulations in the stratification. Since the departure from the plane-averaged velocity forms closed circulation cells, we refer to these features as "rolls," although note that the isopycnals associated with these features do not overturn and hence these features could instead be referred to as "waves."

These features qualitatively match the description of roll-like structures that emerge following linear instabilities in Ekman layer velocity profiles (Lilly 1966; Faller and Kaylor 1966; Brown 1972; Deusebio et al. 2014; Mkhinini et al. 2013). In laboratory experiments and simulations of steady, unstratified flow the Ekman rolls remained almost stationary with and parallel to the imposed current (Lilly 1966; Faller and Kaylor 1966). Strong stabilizing stratification can turn the angle of the Ekman rolls further from the imposed current orientation and allow the rolls to propagate with the imposed current (Brown 1972).

In the LES here, there was weak stabilizing stratification from ice melting and strong oscillating flow from the tides. The Ekman rolls appeared to be mainly stationary in angle but were translated in the slope-parallel directions (back and forth) by the changing tide. The Ekman rolls were not always present in time, generally forming at the weaker currents in the spring–neap tidal cycle. For stronger currents, especially when there was a rapid change in current direction, there was more turbulence and Ekman rolls were no longer a strong feature. In the remainder of this section we investigate these Ekman rolls more quantitatively.

The energy in the rolls can be quantified by calculating the turbulent kinetic energy (TKE) in wavenumber space. The Ekman rolls exhibited significant 2D structure in the slope-parallel directions, hence a 2D slice at 20-m depth was chosen to investigate the rolls in wavenumber space, as shown in Fig. 7 for day 70. The TKE maximum resided in wavenumbers consistent with the Ekman roll structures in Fig. 6, corresponding to dimensionless wavenumbers $kL/2\pi = 3$ and $lW/2\pi = 5$ for day 70, where k and l are the dimensional wavenumbers and L and W are the domain sizes in the x and y directions, respectively. To examine the size and orientation of the rolls, we chose a minimum value of the TKE to define a cutoff envelope. For values within the envelope, the wavenumbers were weighted by the TKE to find the average k and l wavenumbers associated with the rolls. The cutoff TKE was chosen as 3×10^{-9} m^2 s^{-2}, which encompassed the majority of the TKE

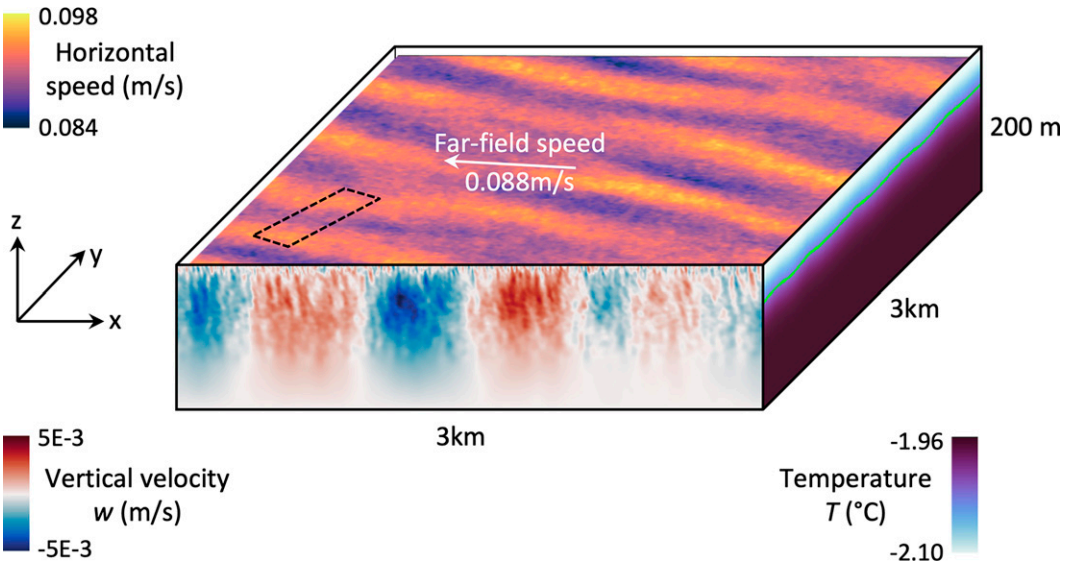

FIG. 6. Snapshot taken at day 70 for the large domain simulation shows the vertical velocity, temperature, and slope-parallel speed of the three-dimensional flow. An isothermal (green line) of $T = -2.02$°C is shown on the vertical slice of temperature. The slope-parallel slice of speed is from 20-m depth, with the far-field speed and orientation also included for this time step (white arrow). The dashed rectangle on the slope-parallel slice demonstrates the size and orientation of the small domain simulation.

peak (green contour in Fig. 7). A sensitivity analysis was conducted to find the best cutoff TKE to capture the TKE peak without including contributions from wavenumbers that were clearly outside the region of interest. The TKE cutoff was applied in wavenumber space to each time, meaning that the green contour varied somewhat in wavenumber space over time, but it was noted to capture the roll activity for the majority of the simulation.

The resulting width and angle of the Ekman rolls over time are shown in Figs. 8b and 8c. The angle was defined with respect to the x direction (the direction of ice base slope) and describes the longitudinal direction of the rolls (i.e., perpendicular to the periodicity in the structures). Figure 8a includes the mean speed at the same depth ($z = -20$ m) to illustrate the timing of the tidal cycle. The roll structures are clearly visible by day 10, where they were approximately 200 m wide and at an angle of 60°, so significantly smaller than the domain size (3 km). As the simulation progressed, the rolls widened while the roll angle stayed about the same. The rolls were aligned roughly parallel to the diurnal tidal ellipse maxima (K_1 and O_1). This was consistent with linear stability theory in which the Ekman rolls aligned parallel to the driving current (Lilly 1966). Interestingly, when the basal slope was not present, the roll width remained around 200 m for almost the entire simulation (appendix C). The mixed layer depth grew at a similar rate regardless of the basal slope and meltwater plume presence (not shown here). This implies that the widening of the Ekman rolls could be the result of some other interaction with the meltwater plume. In other words, even though the stratification was similar between simulations with and without ice base slope, in the former case the meltwater could drive flow and hence change the shear and Ekman roll width.

The cutoff envelope was also used to calculate the fraction of the total TKE associated with the rolls (Fig. 8d). The rolls were responsible for more than half of the total TKE at all times. In general, the rolls were less well defined (a smaller fraction of the TKE) during times with a strong tidal current. This could be due to more shear turbulence at the large flow speeds (especially when there was a sudden change in speed) resulting in the breakup of the rolls.

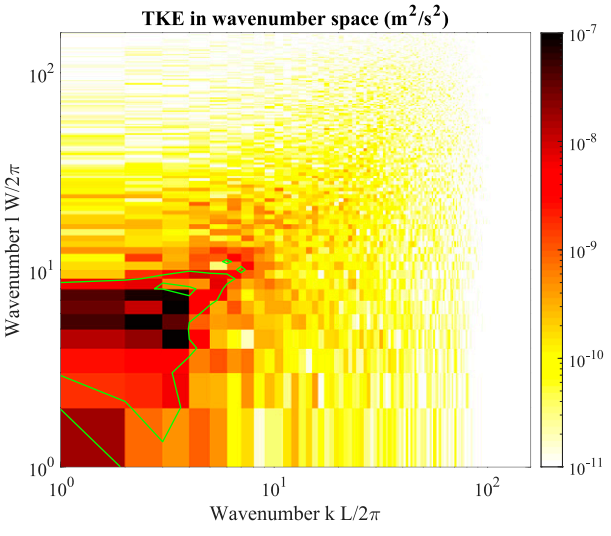

FIG. 7. Turbulent kinetic energy in wavenumber space (k, l). The TKE was calculated from a slope-parallel slice of velocity corresponding to the same time and depth shown in Fig. 6 (day 70, $z = -20$ m). Velocity fluctuations were taken with respect to values averaged in the slope-parallel directions. The green contour shows the chosen cutoff TKE = 3×10^{-9} m^2 s^{-2}.

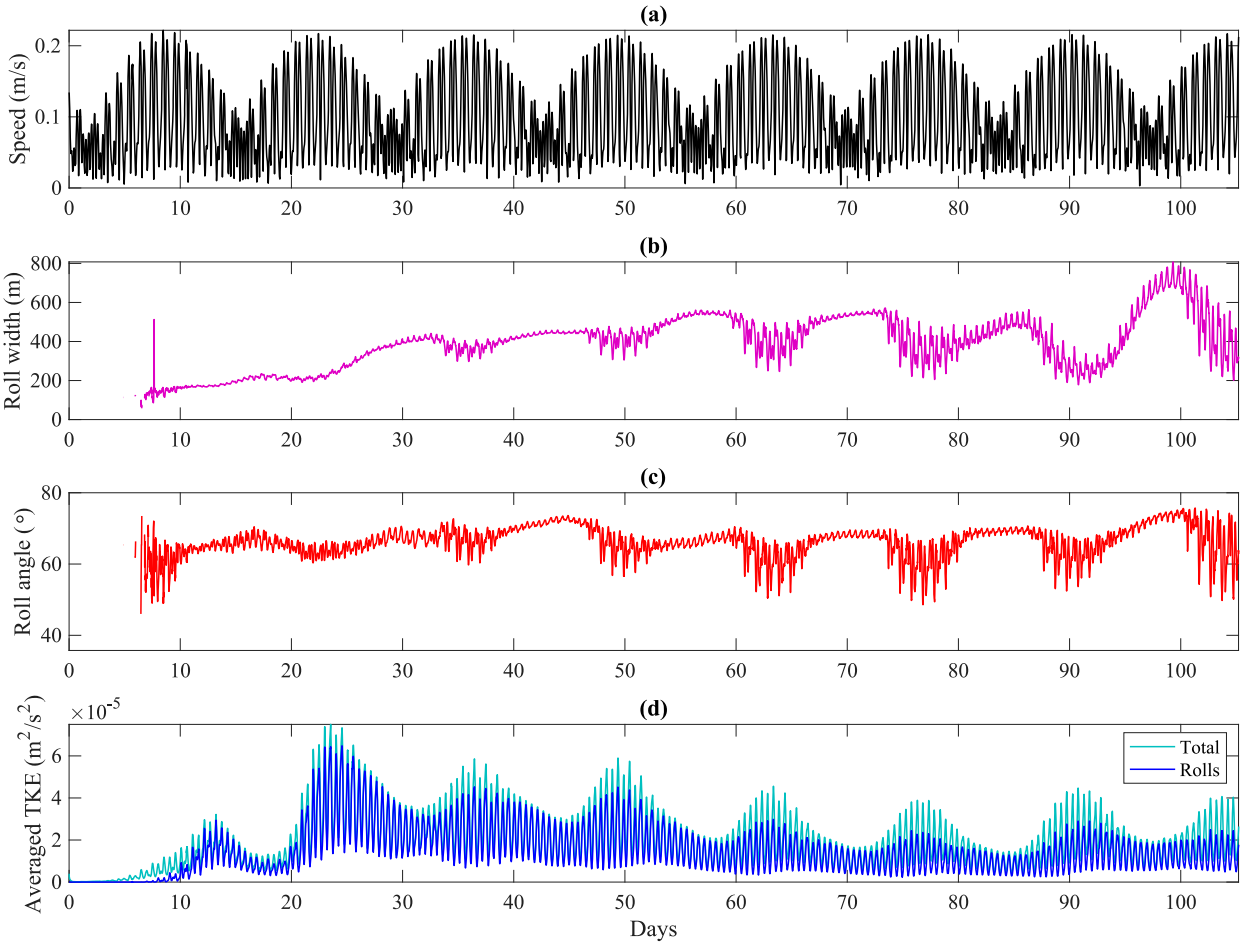

FIG. 8. The evolution of the Ekman rolls at depth $z = -20$ m. (a) Mean current speed of the flow at $z = -20$ m, (b) roll width, (c) roll angle, and (d) averaged turbulent kinetic energy TKE. The TKE has been averaged across the slope-parallel slice at $z = -20$ m for each time step. The total of this average TKE is shown, along with the portion associated with the Ekman rolls. The Ekman roll portion of TKE was calculated using the chosen cutoff in wavenumber space (cut off value of TKE = 3×10^{-9} m^2 s^{-2} for the large domain grid resolution).

c. *Turbulence*

The influence of small-scale turbulence on the vertical heat flux and melt rate will now be investigated using the high-resolution simulation in the small domain where more of the small-scale turbulence was directly resolved. This simulation also provided a test of the resolution dependence of the LES results. The relatively large Ekman rolls presented a challenge when setting up the simulation in a small domain with periodic boundary conditions. To overcome this challenge, the small computational domain (x', y', z) was aligned with the dominant angle of the Ekman rolls, as shown in Fig. 6. The small domain could therefore capture one 600-m-wide Ekman roll based on the roll width at day 52 in the large domain simulation. To reduce the computational cost, a smaller domain size of 200 m was used in the direction parallel to the Ekman rolls. The small domain simulation was initialized from mean profiles taken at day 52 of the large domain simulation (interpolated onto the finer grid). For comparison, an additional simulation of the large domain was also initialized from mean profiles taken at day 52: this will be the large domain (low resolution) simulation used for all comparisons in this subsection. The small domain simulation, along with the reinitialized large domain simulation, were run for 30 days.

The three-dimensional snapshot at day 70 in Fig. 9 shows that the rolls clearly aligned with the domain, but rather than one 600-m-wide roll, there were three 200-m-wide rolls. One explanation was that the Ekman rolls first form through an instability at the wavenumber corresponding to 200 m. The rolls remained 200 m wide in the small domain simulation. In comparison, the reinitialized large domain simulation also formed 200-m-wide rolls until day 68 where they grew in size to around 600 m (not shown here). This suggests that the size of the Ekman rolls might be sensitive to the time history of the flow and the larger-scale motions not captured in the small domain. Figure 9 also shows a layer of small-scale turbulence immediately beneath the ice base.

The majority of the mixed layer heat flux in the small domain simulation was due to resolved turbulence. Figure 10 shows vertical profiles of the SGS diffusivity κ_{SGS} (Fig. 10a) and of the resolved and SGS components of the heat flux for the large (Fig. 10b) and small (Fig. 10c) domain simulations. In the small domain simulation, κ_{SGS} was roughly a quarter of

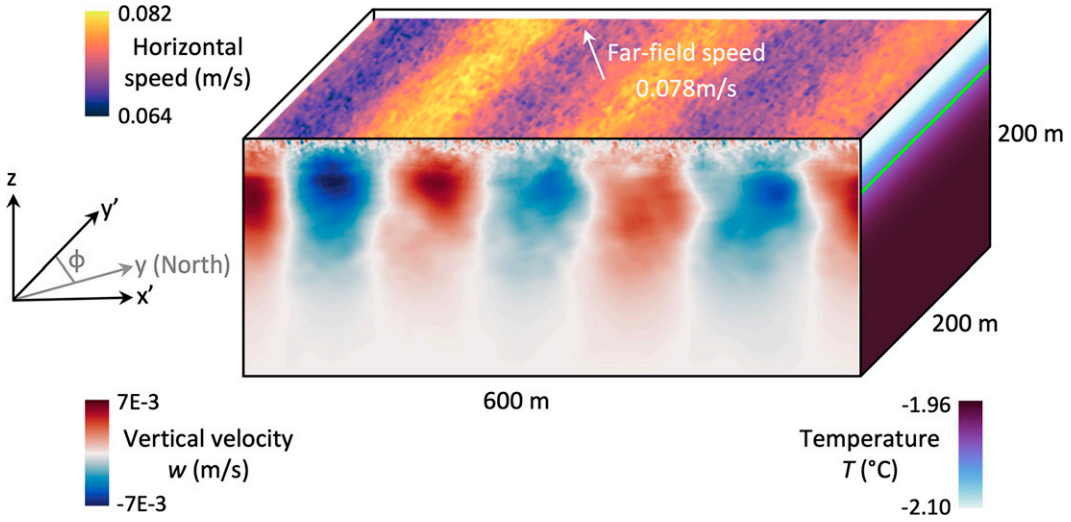

FIG. 9. Snapshot taken at day 70 for the small domain simulation shows the vertical velocity, temperature, and slope-parallel speed of the three-dimensional flow. An isothermal (green line) of $T = -2.02°C$ is shown on the vertical slice of temperature. The slope-parallel slice of speed is from 10-m depth, with the far-field speed and orientation also included for this time step (white arrow).

that in the large domain case (Fig. 10a). The chosen SGS model (the anisotropic minimum-dissipation model) calculated κ_{SGS} for each grid cell and time step using the three-dimensional velocity and temperature fields. Smaller values of κ_{SGS} meant that the resulting SGS contribution to the total vertical heat flux was reduced for the small domain simulation (Figs. 10b,c). Interestingly, the resolved heat flux contribution was only a little larger for the small domain simulation. For the large domain simulation, the heat flux was strongly dominated by the SGS contribution, leading to a large total heat flux. As the small domain simulation saw a big decrease in the SGS contribution and only a small increase in the resolved portion, this led to an overall reduction in the total heat flux compared to the large domain simulation, which will be explored further later in this section.

Continuing with the analysis of the small domain simulation, the time evolution of total TKE and heat transport associated with flow at different depths (10 and 20 m), along with the roll contribution, is shown in Fig. 11. The TKE and vertical heat flux were calculated using a 2D x'-direction slice of velocities and temperature for each depth in wavenumber–depth space (not shown here). In wavenumber–depth space, the TKE was strongest at wavenumber $k'L/2\pi = 3$ (consistent with the three Ekman rolls in Fig. 9) and the depth of maximum TKE fluctuated between 20 and 30 m with the changing tidal currents. The partitioning into the roll contribution in Fig. 11 used the TKE cutoff of 6×10^{-6} m^2 s^{-2}, which was equivalent to the TKE cutoff used in Figs. 7 and 8 for the large domain simulation but renormalized for the small domain dimensions.

The resulting TKE evolution shows a time offset between 10- and 20-m depth (Figs. 11b,d). At 10 m there was an envelope of larger TKE (less than half of which lies with the Ekman rolls) that matched the timing of the driving tidal forcing, though with a slight lag from the far-field flow (Fig. 11a). This is consistent with the fluctuations at 10 m being shear turbulence associated with the tidal forcing. For the 20-m depth, the envelope with larger TKE occurred after the maximum tidal forcing and was almost entirely associated with the Ekman rolls. The timing of the Ekman rolls at 20-m depth is consistent with the timing of the roll component of the TKE at 10-m depth, meaning that it was the rolls that lagged the tidal envelope. There was more total heat flux at 10 m (Figs. 11c,e), which matches the time-averaged depth profiles of heat flux contributions in Fig. 10 (recall that the total heat flux was comprised of the resolved plus the subgrid-scale contributions). The Ekman rolls were responsible for only a tiny portion of the total heat flux, both at 10 and 20 m, as shown in the cumulative sum of heat flux in Fig. 11f. The implication is then that the heat flux was dominated by higher wavenumbers, so smaller physical scales. Even though Ekman rolls contributed strongly to the TKE, they were only directly responsible for a small amount of vertical heat transport. Of course, the rolls could still be important for the heat transport in a more indirect manner, for example, by driving smaller-scale features that then mix the heat vertically. But so far there is no clear link between the rolls and the vertical heat transport.

For the small domain simulation, the vertical profiles of T–S show that the upper water column became more well mixed while the stratification below tended to sharpen (Fig. 12). Interestingly, the small domain (high resolution) simulation did not match the Larsen C Ice Shelf observed profiles as well as the large domain (low resolution) simulation. This could be indicative of additional processes that have not been explicitly included in the simulations (further discussion in section 4). The melt rate was smaller for the small domain simulation (0.136 m yr^{-1} time averaged over days 65–75) compared to the large domain simulation (0.280 m yr^{-1} time averaged over days 65–75). The mixed layer did not significantly deepen during the small domain simulation, while the large domain

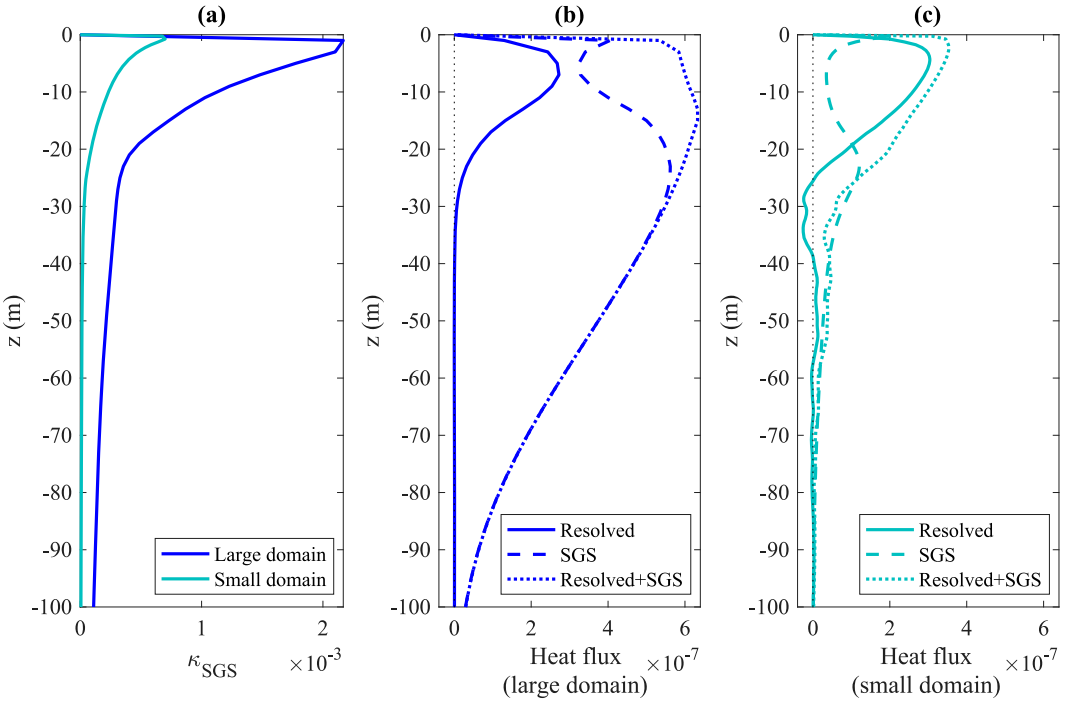

FIG. 10. The resolved vs subgrid-scale contributions for the vertical heat flux at different depths. (a) The subgrid-scale heat diffusivity κ_{SGS} for the large (low resolution) and small (high resolution) domain simulations. The vertical heat flux of the resolved and subgrid-scale contributions for (b) the large domain and (c) the small domain. All values have been averaged in the slope-parallel directions across the domain, and averaged in time for the duration of the re-initialized simulations (from day 52 to day 78). Note that results are shown for the top 100 m only, and that the zero line is plotted in (b) and (c) as a thin black dotted line.

simulation showed a deepening of the mixed layer (from 30- to 34-m depth). This was consistent with the previous results (such as Fig. 10) that show a reduction in heat flux toward the ice base in the small domain simulation.

In conclusion, the small domain simulation saw a modest increase in resolved heat transport due to the higher resolution, but the total heat transport was reduced because of a smaller subgrid-scale contribution. While the Ekman rolls were correlated with around half of the total turbulent kinetic energy, they were not directly responsible for significant heat transport. Overall, the reduced mixing in the small domain simulations resulted in less heat transport toward the ice base, a stagnating mixed layer depth, and a reduction in the melt rate.

4. Discussion

a. Application of results to the ocean

The Ekman rolls are robust features of the large-eddy simulations. To the authors' knowledge, this is the first time that these features have been seen in simulations or observations of under ice shelf flow. In observations, the Ekman rolls may be present but as yet unidentified. To predict how the Ekman rolls signature may appear in borehole measurements, the large domain simulation was sampled at a single point at 20-m depth every 16 s and a wavelet analysis applied to the resulting signal (Fig. 13). There was a likely signature of Ekman rolls in the temperature wavelet analysis with a period of about 1 h, consistent to intervals where the Ekman rolls were observed in the 3D flow field. This period corresponded to the movement of a roll through the measurement location. This was heavily dependent on the tidal current speed, but for intervals when the tidal current was mostly in one direction for 12 h or so there was a corresponding increase in the Ekman roll signature. This signature also clearly appeared in the velocity wavelet analysis (not shown here). Unfortunately this period was not sampled in the DN19 observations, but in the future, it might be possible to identify Ekman rolls with a different sampling strategy.

In the ocean there are other sources of variability that may not be present in the LES. The small domain simulation produced temperature and salinity profiles, and a melt rate, that were further away from the observations than the large domain results. The rapid cooling and lack of stratification in the mixed layer in the small domain simulation suggests that the heat in the mixed layer was consumed too rapidly relative to its supply. This then implies that there was a supply of heat to the mixed layer that was missing: either vertical mixing being too weak or an absence of lateral heat advection. There is evidence that lateral advection was present in the observations (discussed further below), so it is likely at least part of the explanation for the additional supply of heat to the mixed layer. A lack of mixing may also be involved, but it is unclear how great a role it will have played. Below we discuss the potential differences between the LES and real ocean.

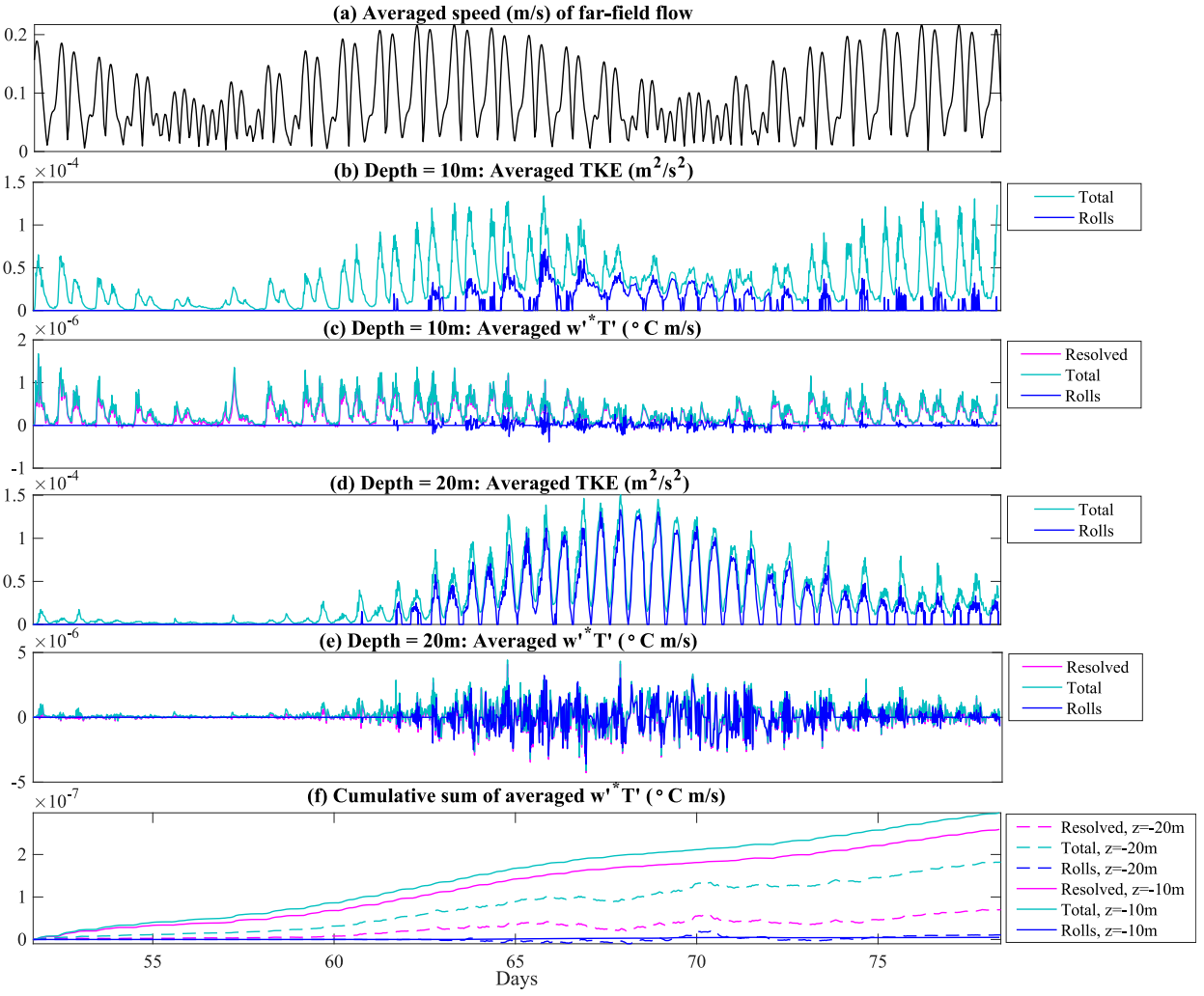

FIG. 11. Partitioning of the turbulent kinetic energy and vertical heat flux into the contribution from the Ekman rolls for the small domain (high resolution) simulation. (a) The slope-parallel averaged speed of the far-field current is included for reference. The averaged (in the x' direction) TKE partitioning is shown for (b) $z = -10$ m and (d) $z = -20$ m. The averaged (in the x' direction) vertical heat flux partitioning is shown for (c) $z = -10$ m and (e) $z = -20$ m. (f) A cumulative sum of the vertical heat flux is shown for both depths. Each panel in (b)–(f) shows the total (cyan) and the component just associated with the Ekman rolls (blue). Also shown in (c), (e), and (f) is the resolved contribution to the vertical heat transport (pink). The cumulative sum in (f) has been normalized so that the final vertical heat flux value equals the time mean across the total interval, for ease of comparison with Fig. 10. The partitioning was done using the TKE cutoff of 6×10^{-6} m^2 s^{-2}, which is equivalent to the TKE cutoff used in Figs. 7 and 8 for the large domain simulation.

One difference between the LES and the ocean was the periodic nature of the simulations in the directions parallel to the ice base. The real-world ocean is not periodic. Neighboring water masses may differ significantly and could feasibly be moved into the domain at different stages of the tidal cycle. There was some evidence for this in the observations, where the T and S profiles significantly cooled and freshened over a brief 7-h interval (Fig. 3). There also could have been additional mixing as the neighboring water mass was transported back and forth, in particular between the far-field flow and the upper mixed layer. Along with different water masses being advected with the tidal cycle, there could also be incoming plume flow from further down the ice shelf. While the observations measure only a weak background flow, even a weak plume from external sources may still have significantly different temperature and salinity than the idealized LES. There is more work to be done to quantify the heat transport from plumes and neighboring currents and how they might impact the stratification of the water column.

Next we consider whether the near-wall model might be responsible for discrepancies in stratification between the simulations and observations. The ice base roughness parameter in the LES was effectively set to zero in the near-wall model. As outlined in appendix B, the Larsen C Ice Shelf observations may have been in a transitionally rough regime. In this regime the ice base roughness may or may not have had some influence on the flow depending on the roughness shape, alignment, and other characteristics (Jiménez 2004). Even so, the

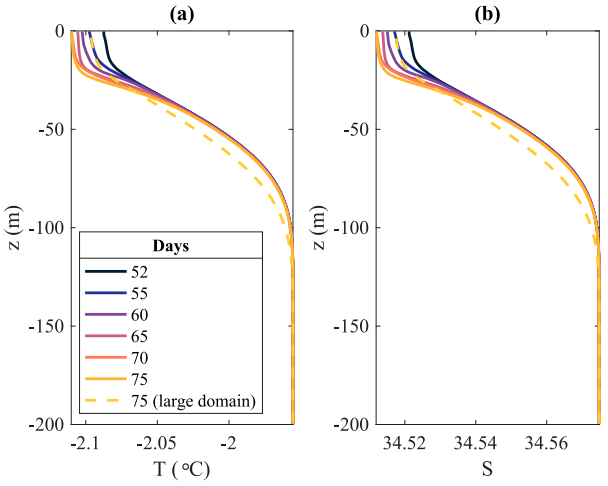

FIG. 12. Vertical profiles of (a) temperature and (b) salinity for the small domain (high resolution) simulation. The simulation profiles are shown at different points in time and have been averaged in the slope-parallel directions across the domain. Note that the topmost values of T, S are from the top of the water column (the first grid cell beneath the ice) rather than being the ice–ocean boundary conditions T_b, S_b.

roughness length scale of 0.4 mm inferred from observations was still relatively minor and not too dissimilar from the smooth ice base in the simulations. There is a caveat that the results from the present simulations demonstrate that the observations may be underestimating (by approximately 25%) the true interfacial stress on which the roughness calculation is based, so the true roughness could be somewhat larger. However, even if the roughness were explicitly included in the near-wall parameterization, the additional turbulence and mixing would be close to the ice base, rather than through the pycnocline where more mixing could transport heat upward into the mixed layer. The small difference in the roughness parameter between the LES and observations is likely not sufficient to explain the lack of heat within the mixed layer (seen in the small domain simulation).

Another explanation for the difference between the small domain LES and the observations is that there may be other sources of mixing that have not been included in the LES. One example is double-diffusive effects due to the large difference in molecular diffusivities between temperature and salinity. There was a faint signature of steps in the observed T–S profiles (30–80-m depth), which may be indicative of double-diffusive layering, where small-scale diffusion across the layer could drive mixing within the layers. The grid spacing of the LES would not have been able to resolve double-diffusive layering, so any additional mixing from this source could explain the difference between the observations and the LES. There also could have been internal waves coming from external sources, which would potentially break and mix regions of the water column beneath the ice base, but so far we do not have any evidence of internal waves breaking in the ocean beneath Larsen C Ice Shelf. Investigating possible sources of mixing is another important area of research at the frontier of ice shelf–ocean interactions.

b. *Three-equation model*

The ice shelf–ocean boundary parameterization of the three-equation model was also examined here using the LES. The heat and salt transfer coefficients calculated with input T and S above the pycnocline (upper 20 m or so beneath the ice) showed almost no variation with flow speed. The drag coefficient C_d calculated with the friction velocity at the ice base and flow speed at 2.5-m depth showed little variation with flow speed. Values of C_d with input flow speeds from 13.5 m and below showed more variation, particularly at low flow speeds. It is worth noting that the drag coefficient might also be expected to vary through time as it is predicted to be a function of stability, and so it may change with the melt rate (i.e., interfacial buoyancy flux). While this was not directly found for Larsen C Ice Shelf here, it may be of importance for ice shelves with higher melt rates.

The LES results demonstrate that it may be acceptable to use the three-equation model with constant coefficients (for Larsen C Ice Shelf or similar) if the first grid point is placed only a few meters from the ice base. Beyond a few meters, the drag coefficient begins to vary more significantly and may cause inaccurate modeling of the melt rate and other parameterized variables. A coarser resolution ocean model using the three-equation model would likely place the first grid point in the mixed layer region (i.e., interacting with the ice). However, a coarse-resolution model is likely to result in an effective mixed layer thickness that is too great with consequently biased properties. Unfortunately, without knowledge of the modeled region, it is difficult to predict a priori the depth of the mixed layer. In coarser ocean models (e.g., cavity-sized models) the entire near-ice region will require parameterization. Some regions of the cavity (e.g., near the grounding line) may be affected by a strong geostrophic plume that drives the boundary layer flow, and in a coarse model this is likely to be missed (Jenkins 2016, 2021; R. D. Patmore et al. 2022, manuscript submitted to *J. Phys. Oceanogr.*). Additional complications are likely to be present for different ice shelves, such as strong stratification, ice base roughness or topography, a more vigorous meltwater plume, and double-diffusive convection.

5. Conclusions

The ocean-driven basal melting of Larsen C Ice Shelf was examined using large-eddy simulations with realistic tides, ice base slope, and Coriolis parameter. We used a new near-wall parameterization to calculate the ice shelf melt rate in the LES. The simulations matched reasonably well with the observed stratification, friction velocity and time-averaged melt rate. One interesting result was that the friction velocity estimated using the covariance method (typically used for in situ observations taken a few meters from the ice) had a time offset with depth and a reduced magnitude with depth. This ultimately shows that the sub-ice upper mixed ocean was not a constant stress boundary layer and that the turbulence generated at the ice base took some time to propagate to depth. Additionally, the instantaneous melt rate was strongly tied to

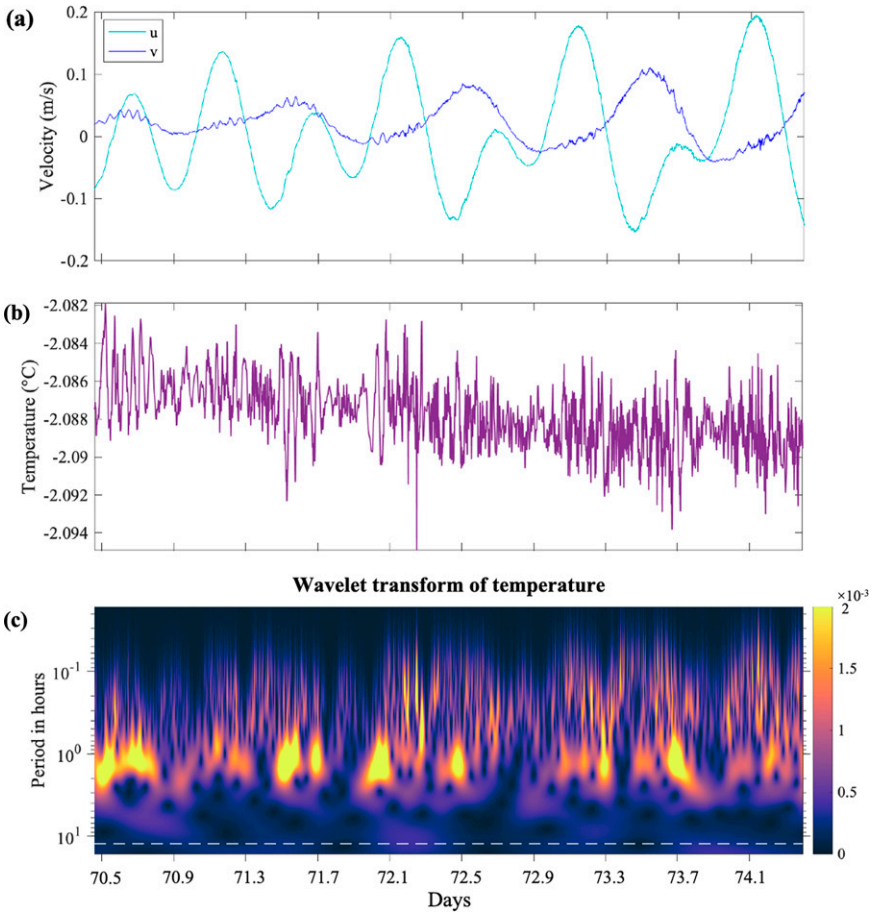

FIG. 13. Time evolution and wavelet analysis for a point measurement at depth $z = -20$ m in the large domain simulation, where the time sampling was approximately 16 s for the interval shown. The point measurement time series of (a) the two slope-parallel velocity components, (b) the temperature, and (c) the resulting wavelet transform for just the temperature measurement. The white dashed line is the M_2 tidal component, and the other two tidal components K_1, O_1 are at periods slightly larger than the interval shown. The wavelet transform uses generalized Morse wavelets with $\gamma = 3$ and $\beta = 2$ [please refer to the jLab MATLAB toolbox by Lilly (2017) for the meaning and detailed discussion of these parameters].

the tidal cycle, which dominated the current speed within the mixed layer immediately beneath the ice.

The simulations also revealed Ekman rolls in the mixed layer and stratified region beneath Larsen C Ice Shelf. While the bulk flow properties were dominated by the tidal forcing, the roll behavior was modified by the presence of the slope, with the roll width slowly increasing over time. The Ekman rolls contributed noticeably to the turbulent kinetic energy but barely affected the vertical heat transport directly. Hence, questions remain on whether it is necessary to include the effects of Ekman rolls in melt rate parameterizations such as the three-equation model.

In terms of the three-equation model, the heat and salt coefficients calculated using temperature and salinity values within the mixed layer (top ~20 m) were largely independent of current speed and were consistent with past observations such as from Ronne Ice Shelf (Jenkins 2011). The drag coefficient C_d at the ice base was nearly constant when considering current speeds close to the ice base (2.5-m depth), but varied significantly when calculated using the current speed below the mixed layer, particularly during intervals with low flow speeds. The LES results caution the use of the three-equation model, in particular with a constant drag coefficient, unless the vertical ocean structure beneath the particular ice shelf site is known a priori.

Although our simulations captured some details of the observations, there were notable differences. In particular, the stratification at the base of the mixed layer in the high-resolution simulation was larger than observed, and the modeled melt rate in this case was smaller than the observations. This suggests that some processes that are not captured in our simulations might be important sources of heat transport. For example, our model setup does not include advection of large-scale temperature and salinity gradients, double diffusion, or a

background internal wave field. It is possible that a more realistic model of the full ice shelf cavity could provide additional insight, in particular on the large-scale advection of water mass properties. Parameter sensitivity studies would also be useful to predict how the results might change in time or differ at other locations. Ultimately, however, additional observations will be needed to identify the processes that control the melt rate. There remains significant work to improve our understanding of ice shelf–ocean interactions and the rich dynamics in these regions.

Acknowledgments. The NERC Standard Grant NE/N009746/1 is gratefully acknowledged for supporting this research. This work used the ARCHER U.K. National Supercomputing Service (http://www.archer.ac.uk).

APPENDIX A

Tidal Forcing Terms for the Momentum Equation

The tidal forcing in the LES was based on the in situ velocity observations taken below Larsen C Ice Shelf by DN19. The strongest tidal components from the observations at 13.5-m depth were chosen (O_1, K_1, M_2) and, by assuming geostrophic balance, a pressure gradient force was calculated. There is a question about how truly geostrophic the velocities are at 13.5-m depth, which might lie within the mixed layer and be influenced by ice base friction and other boundary dynamics. But as these data are the most comprehensive information available on the Larsen C Ice Shelf tidal velocities, they are used to force the model.

To derive the tidal forcing F_x, F_y in Eq. (4) we solved the time variant geostrophic equations,

$$\frac{du}{dt} - fv = F_x, \quad \frac{dv}{dt} + fu = F_y. \tag{A1}$$

Rewriting F_x, F_y with the three chosen tidal components, $F_x = F_{x,O_1} + F_{x,K_1} + F_{x,M_2}$ and $F_y = F_{y,O_1} + F_{y,K_1} + F_{y,M_2}$. Considering just the O_1 tidal components, the u_{O_1} and v_{O_1} velocities are

$$\begin{aligned} u_{O_1} &= A_{u,O_1} \cos(\omega_{O_1} t_{\text{tide}} - \Phi_{u,O_1}), \\ v_{O_1} &= A_{v,O_1} \cos(\omega_{O_1} t_{\text{tide}} - \Phi_{v,O_1}), \end{aligned} \tag{A2}$$

where A is the amplitude, $\omega = 2\pi/T$ is the tidal frequency, T is the tidal period, and Φ is the phase lag. The time $t_{\text{tide}} = t - t_{\text{central}}$ is relative to the central nodal time used to compute the observed constituents which is approximately half a year, $t_{\text{central}} = 182.5$ days $= 1.58 \times 10^7$ s. Substitute Eqs. (A2) into Eqs. (A1) to find

$$\begin{aligned} F_{x,O_1} = &- A_{u,O_1} \omega_{O_1} \sin(\omega_{O_1} t_{\text{tide}} - \Phi_{u,O_1}) \\ &- A_{v,O_1} f \cos(\omega_{O_1} t_{\text{tide}} - \Phi_{v,O_1}), \end{aligned} \tag{A3}$$

$$\begin{aligned} F_{y,O_1} = &- A_{v,O_1} \omega_{O_1} \sin(\omega_{O_1} t_{\text{tide}} - \Phi_{v,O_1}) \\ &+ A_{u,O_1} f \cos(\omega_{O_1} t_{\text{tide}} - \Phi_{u,O_1}), \end{aligned} \tag{A4}$$

TABLE A1. Constants used in the tidal forcing terms in the LES, based on DN19 observed values. The amplitudes have been multiplied by a factor of 1.3 to result in maximum speeds that are on par with the observed values. Also note that we have converted DN19's tidal ellipse parameters into tidal amplitude and phase lag to use here.

Mode	A_u (m s^{-1})	A_v (m s^{-1})	Φ_u (rad)	Φ_v (rad)	ω (rad s^{-1})
O_1	7.00×10^{-2}	4.68×10^{-2}	1.038	3.80	6.76×10^{-5}
K_1	8.26×10^{-2}	4.46×10^{-2}	2.51	5.41	7.29×10^{-5}
M_2	8.23×10^{-2}	1.51×10^{-2}	4.79	3.50	1.41×10^{-4}

and F_{x,K_1}, F_{y,K_1}, F_{x,M_2}, and F_{y,M_2} follow the same form. The respective constants are based on values from DN19, see Table A1. The strongest three measured tidal components resulted in replicating important characteristics such as a regular spring–neap cycle, but did not quite result in the same maximum amplitudes of speed that were sometimes present in the observations. To ensure that these maximum amplitudes were well represented in the simulations, a multiplication factor of 1.3 was used in the tidal forcing.

APPENDIX B

Near-Wall Model for the Ice Melting Boundary Condition

a. Derivation of the near-wall model

To derive the near-wall model algorithm, let us first review the Monin–Obukhov similarity theory for stratified flow. This theory relates the gradients in velocity, temperature, and salinity by the common Monin–Obukhov functions Φ_m and Φ_s. In other words, the gradient profiles are expected to be similar in shape. The Monin–Obukhov similarity equations for velocity, temperature and salinity are

$$\frac{\partial U}{\partial z} = \frac{u_*}{k_m z}\Phi_m(\xi), \quad \frac{\partial T}{\partial z} = \frac{T_*}{k_s z}\Phi_s(\xi), \quad \frac{\partial S}{\partial z} = \frac{S_*}{k_s z}\Phi_s(\xi), \tag{B1}$$

where U is the speed, $u_* = \sqrt{\nu|\partial U/\partial z|_b}$, $T_* = \kappa_T|\partial T/\partial z|_b/u_*$, and $S_* = \kappa_S|\partial S/\partial z|_b/u_*$ are the friction velocity, temperature, and salinity, respectively. The subscript b indicates variables at the ice–ocean boundary. The von Kármán constants for the momentum and scalars are, respectively, $k_m = 0.41$ and $k_s = 0.48$ (Bradshaw and Huang 1995). The Monin–Obukhov functions Φ_m and Φ_s are functions of the normalized distance from the ice $\xi = z/L$. The Obukhov length,

$$L = -\frac{u_*^3}{k_m B}, \tag{B2}$$

describes the relative strength of turbulence compared to stratification, where the vertical buoyancy flux at the ice–ocean interface is $B = g(\alpha\kappa_T|\partial T/\partial z|_b - \beta\kappa_S|\partial S/\partial z|_b)$. The Obukhov length can be thought of as the distance away from the ice, above which we might expect turbulence to dominate

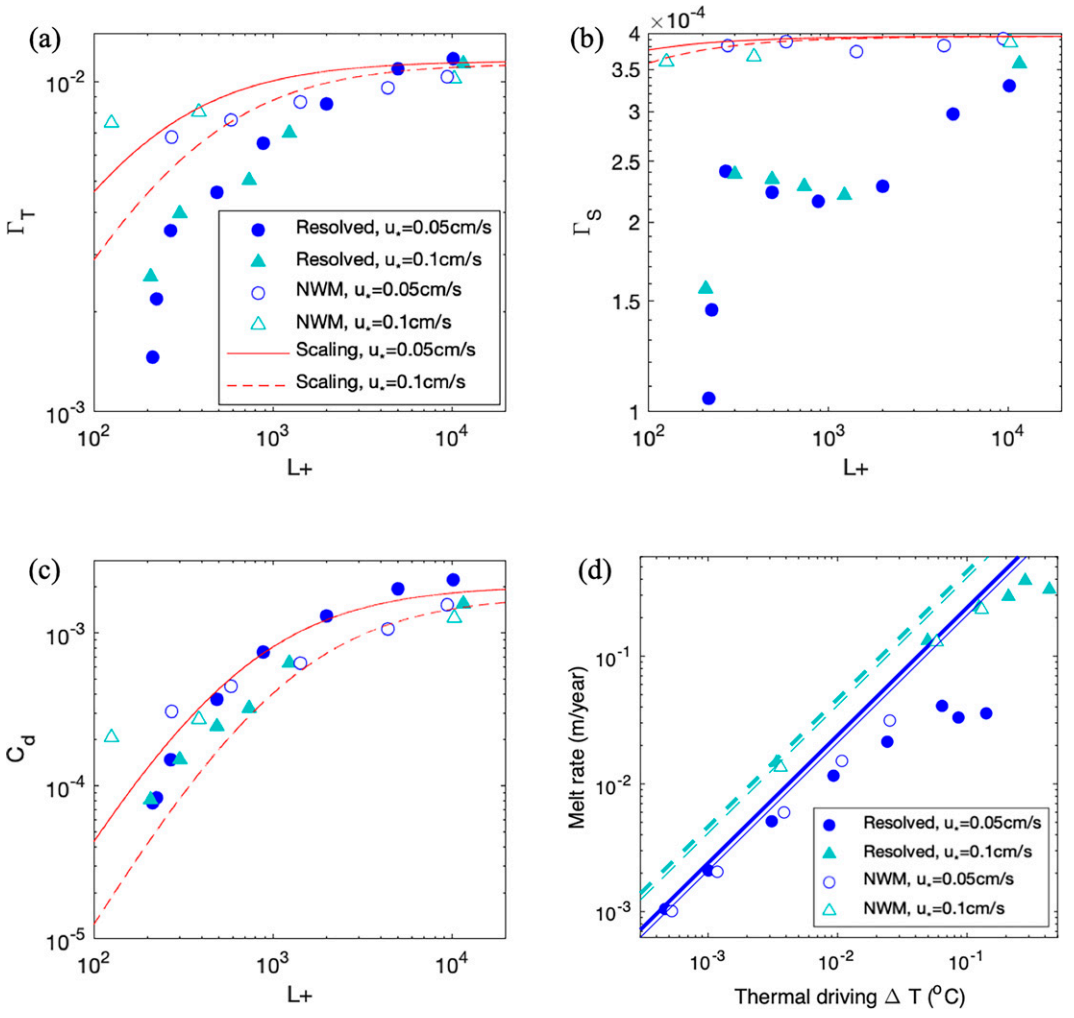

FIG. B1. Near-wall model (NWM) validation: transfer coefficients of (a) heat Γ_T and (b) salt Γ_S, and (c) drag coefficient C_d [Eq. (B14)] against Obukhov length scale ratio L^+, and (d) melt rate against thermal driving $\Delta T = T_{z=-2\mathrm{m}} - T_b$. The results from resolved LES of the upper 2 m below the ice base reported in Vreugdenhil and Taylor (2019) are shown as the solid symbols (and thick lines), and results using the derived near-wall model with the first grid point within the log layer (8 cm from base of the ice) are shown as the open symbols (and thin lines). Colors show two different friction velocities. Solid lines are $u_* = 0.05\,\mathrm{cm\,s^{-1}}$ cases, and dashed lines are $u_* = 0.1\,\mathrm{cm\,s^{-1}}$ cases. In (a)–(c), the red lines show the Monin–Obukhov scaling that the near-wall model is based on. The lines in (d) correspond to the passive scalar limit.

the flow, and below which the effects of stratification will be important.

To better understand these Monin–Obukhov functions, let us consider the case where the flow has a very low interfacial buoyancy flux, which we refer to as a very weakly stratified case. If stratification is very weak then the Obukhov length L becomes very large, and the normalized distance from the wall ξ becomes small. As L is far from the wall, the majority of the flow is unaffected by stratification and we would expect $\Phi_m = \Phi_s = 1$. This results in Eq. (B1) reverting to the well-known law-of-the-wall logarithmic scaling with no stratification term (Pope 2000).

If stratification is stronger then it can start affecting the turbulence in the flow. In particular, we would expect strong stabilizing stratification to damp out some or all of the shear turbulence. The frictional Obukhov length $L^+ = L/(\nu/u_*)$ is one measure of the transition to turbulent flow. When $L^+ > 200$ the flow is predicted to be fully turbulent. However, the form of the stratified Monin–Obukhov function is still contested (e.g., Businger et al. 1971; Kaimal et al. 1976; Foken 2006). One straightforward and common form is of a linear function of ξ,

$$\Phi_m(\xi) = 1 + \beta_m \xi, \quad \Phi_s(\xi) = 1 + \beta_s \xi, \tag{B3}$$

where $\beta_m = 4.8$ and $\beta_s = 5.6$ are constants (Wyngaard 2010; Zhou et al. 2017). Here, we will use the linear function Eq. (B3) to derive our near-wall model. By vertically integrating Eq. (B1) we find

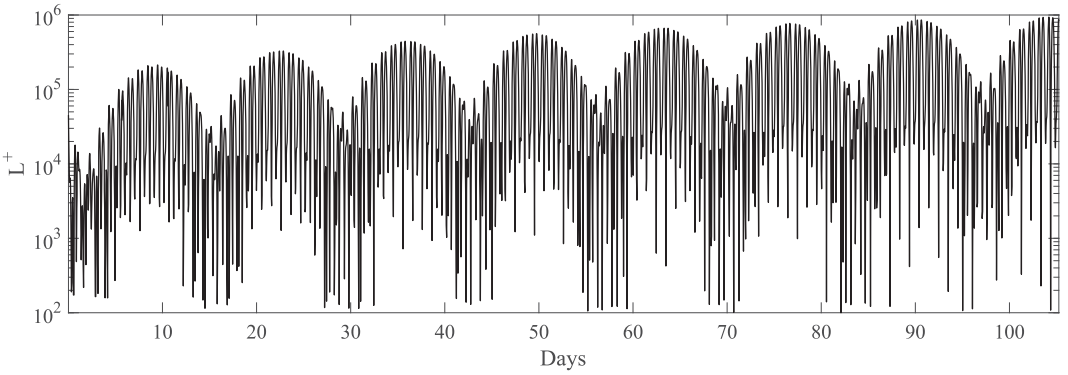

FIG. B2. The Obukhov length scale ratio L^+ with time for the large domain near-wall model LES.

$$\frac{U(z_g)}{u_*} = \frac{1}{k_m}\ln\left(\frac{z_g u_*}{\nu}\right) + \frac{\beta_m}{k_m}\xi(z_g) + 5, \tag{B4}$$

$$\frac{T(z_g) - T_b}{T_*} = \frac{1}{k_m}\ln\left(\frac{z_g u_*}{\nu}\right) + \frac{\beta_m}{k_m}\xi(z_g) + (13\mathrm{Pr}^{2/3} - 7.5), \tag{B5}$$

$$\frac{S(z_g) - S_b}{S_*} = \frac{1}{k_m}\ln\left(\frac{z_g u_*}{\nu}\right) + \frac{\beta_m}{k_m}(z_g) + (13\mathrm{Sc}^{2/3} - 7.5), \tag{B6}$$

where the final terms on the right hand side are integration constants that describe the thickness of the viscous, heat diffusive, and salt diffusive sublayers. These terms are set following past work on boundary layer turbulence (Bradshaw and Huang 1995; Schlichting and Gersten 2003), stratified plane Couette flow (Deusebio et al. 2015; Zhou et al. 2017), and ice melting studies (Kader and Yaglom 1972; McPhee et al. 1987; Holland and Jenkins 1999; Vreugdenhil and Taylor 2019). Note that we have evaluated the Eqs. (B4)–(B6) for the input values of temperature, salinity, and velocity to be those in the first grid cell in the domain, designated by the depth subscript g.

A smooth ice base has been assumed by including the viscous length scale in the first term on the RHS of Eqs. (B4)–(B6), this could be replaced with a roughness length scale if there was significant roughness on the ice base. In the DN19 Larsen C Ice Shelf observations the measured drag coefficient was on average 0.0022 (for Upper MAVS flow at speeds > 0.1 m s^{-1}), which gave a roughness length scale of 0.4 mm. This roughness length scale is expected to be approximately 1/30 of the vertical amplitude of the roughness elements, which is then $k_r = 12$ mm (Jiménez 2004). A useful measure of the roughness effect on the flow is the roughness Reynolds number $\mathrm{Re}_r = k_r u_*/\nu$ (Jiménez 2004). The roughness Reynolds number for Larsen C Ice Shelf base is $\mathrm{Re}_r = 32$ (using $u_* = 0.0047$ m s^{-1} associated with $U = 0.1$ m s^{-1}, and $\nu = 1.8 \times 10^{-6}$ m^2 s^{-1}). This places the ice base in the transitional roughness regime (between approximately $4 < \mathrm{Re}_r < 80$) where roughness may start having an effect on the flow depending on the roughness shape, alignment, and other characteristics (Jiménez 2004). This minor roughness was not too dissimilar from the smooth ice base in the simulations.

In past resolved LES the temperature, salinity and velocity profiles were well described by Monin–Obukhov similarity scaling for stratified flow [Eqs. (B4)–(B6)], provided that the flow was not too strongly stratified i.e., $L^+ > 200$ (Vreugdenhil and Taylor 2019). This is thought to be the appropriate regime for the strongly turbulent and weakly stratified ocean beneath Larsen C Ice Shelf.

Next we review the diffusive three-equation model for ice melting. The three equations are the conservation of heat and salt across the ice–ocean boundary, and the liquidus condition which describes the phase change of ice to liquid water, respectively,

$$c_w \rho_w u_* T_* = \rho_i L_i m, \tag{B7}$$

$$\rho_w u_* S_* = \rho_i S_b m, \tag{B8}$$

$$T_b = \lambda_1 S_b + \lambda_2 + \lambda_3 P, \tag{B9}$$

where m is the melt rate and T_b and S_b are the temperature and salinity at the ice–ocean boundary (McPhee et al. 1987; Holland and Jenkins 1999). Recall that u_* is the interfacial momentum flux or friction velocity, and T_* and S_* are the interfacial heat and salt fluxes (normalized by the friction velocity). The subscript w refers to values for water and i for ice. The specific heat capacity for water is $c_w = 3974$ J kg^{-1} °C^{-1} and the latent heat of fusion is $L_i = 3.34 \times 10^5$ J kg^{-1}. The coefficients in the linearized expression for the freezing point of seawater are $\lambda_1 = -5.73 \times 10^{-2}$ °C, $\lambda_2 = -8.32 \times 10^{-2}$°C, and $\lambda_3 = -7.53 \times 10^{-4}$°C dbar (Jenkins 2011). Finally, the background pressure due to the ice depth $P = 304$ dbar is chosen to match Larsen C Ice Shelf. Following from previous studies using the diffusive three-equation model, we have assumed that the volume input of water due to ice melting, the salinity of ice, and the conduction of heat through the ice are all zero (Gayen et al. 2016; Mondal et al. 2019; Vreugdenhil and Taylor 2019).

For our near-wall model we now have six equations [Eqs. (B4)–(B9)] and six unknowns (u_*, T_*, S_*, m, T_b, S_b)

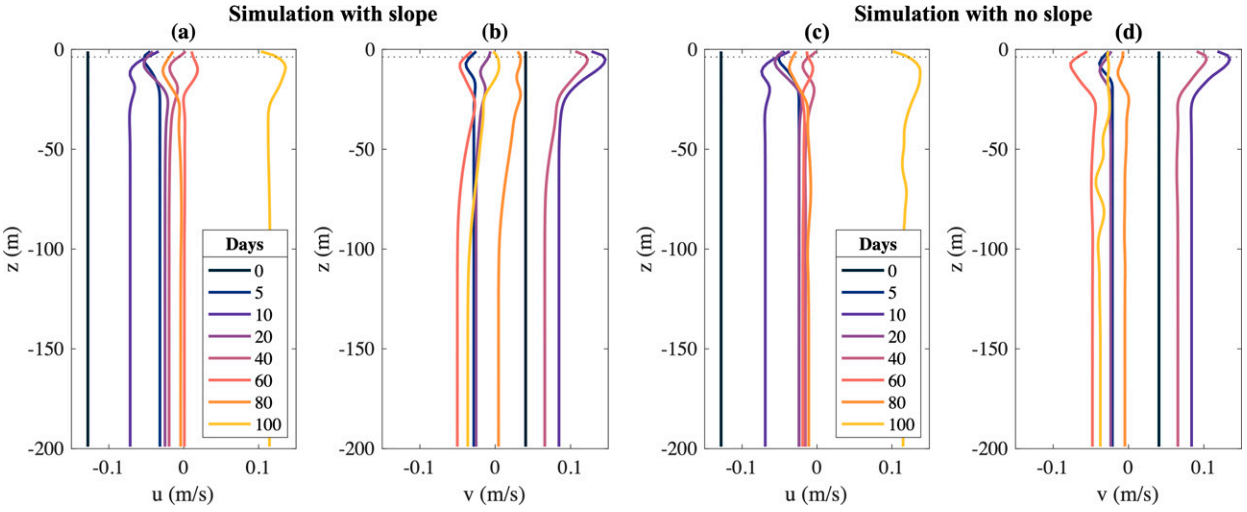

FIG. C1. Vertical profiles of slope-parallel velocity (a),(c) u and (b),(d) v for the simulations with (a),(b) ice base slope and (c),(d) no slope. The simulation profiles are shown at different points in time and have been averaged in the slope-parallel directions across the domain. The dotted lines show the Ekman layer depth, $\sqrt{2\nu_{\mathrm{SGS}}/f}$, where $\nu_{\mathrm{SGS}} \approx 10^{-3}$ m^2 s^{-1} was the maximum turbulent viscosity. Note that the topmost values of u, v are from the first grid cell beneath the ice rather than being the ice–ocean boundary conditions which are no-slip (zero u, v).

when driven by the external forcing conditions $T(z_g)$, $S(z_g)$, and $U(z_g)$. The equations are solved using the multivariate Newton–Raphson iteration method. This method uses a first guess based on the previous time step, then with each iteration reduces the residual error, eventually converging on a solution. The Newton–Raphson iteration method can become computationally expensive, depending on the number of iterations required for the solution to converge. To save on computer time, for each time step we solve Eqs. (B4)–(B9) with the slope-parallel averaged temperature $T(z_g)$, salinity $S(z_g)$, and speed $U(z_g)$ at the first grid cell inside the domain. This spatial averaging follows from work on using the Monin–Obukhov scaling to parameterize the effects of the atmospheric boundary layer (e.g., Moeng 1984). Once we have the solution for the slope-parallel averaged values, for each boundary grid cell we scale the solution by the local values of velocity, temperature, and salinity. For the velocities the stress component is partitioned into the streamwise and spanwise slope-parallel velocity components following Piomelli et al. (1989). We note that our overall approach is similar to methods previously used for Monin–Obukhov similarity theory applied to the atmospheric boundary layers for one scalar (temperature) (e.g., Businger et al. 1971), which we have simply added in complexity in the form of two scalars (temperature and salinity) that then have a complicated relationship through the diffusive three-equation model. The resulting locally scaled solutions are

$$\tau_{13}(x,y,z=0) = \frac{u(x,y,z_g)}{U(z_g)}\,\tau_w, \tag{B10}$$

$$\tau_{23}(x,y,z=0) = \frac{v(x,y,z_g)}{U(z_g)}\,\tau_w, \tag{B11}$$

$$T_*(x,y,z=0) = \frac{T(x,y,z_g) - T_b}{T(z_g) - T_b}\,T_*, \tag{B12}$$

$$S_*(x,y,z=0) = \frac{S(x,y,z_g) - S_b}{S(z_g) - S_b}\,S_*, \tag{B13}$$

where $\tau_w = \rho_0 u_*^2$ is the wall shear stress. These can then be applied as flux boundary conditions in the large-eddy simulations.

b. Validation of the near-wall model

The near-wall model was validated by comparing coarse resolution LES (with the near-wall model) against resolved LES (which explicitly resolved the viscous and diffusive sublayers) from Vreugdenhil and Taylor (2019). For both LES, the domain was the top 2 m of the water column. A constant pressure differential was imposed to drive flow and two different pressure differentials were investigated that resulted in two different friction velocities. A range of thermal driving $\Delta T = T_{z=-2\mathrm{m}} - T_b$ was also covered. The coarse-resolution LES had 8-cm grid spacing in the vertical direction, which also determined the depth of the first grid point.

For the validation comparison, variables of interest are the heat Γ_T and salt Γ_S transfer coefficients and the drag coefficient C_d calculated as

$$\Gamma_T = \frac{T_*}{T(z) - T_b}, \quad \Gamma_S = \frac{S_*}{S(z) - S_b}, \quad C_d = \left[\frac{u_*}{U(z)}\right]^2. \tag{B14}$$

Written in this form, it is clear that there is a direct link between the transfer coefficient definition [Eqs. (B14)] and the Monin–Obukhov scaling [Eqs. (B4)]. As the Monin–Obukhov scaling is a part of the near-wall model, it is instructive to determine whether the transfer coefficients (output from the near-wall model) deviate from the scaling

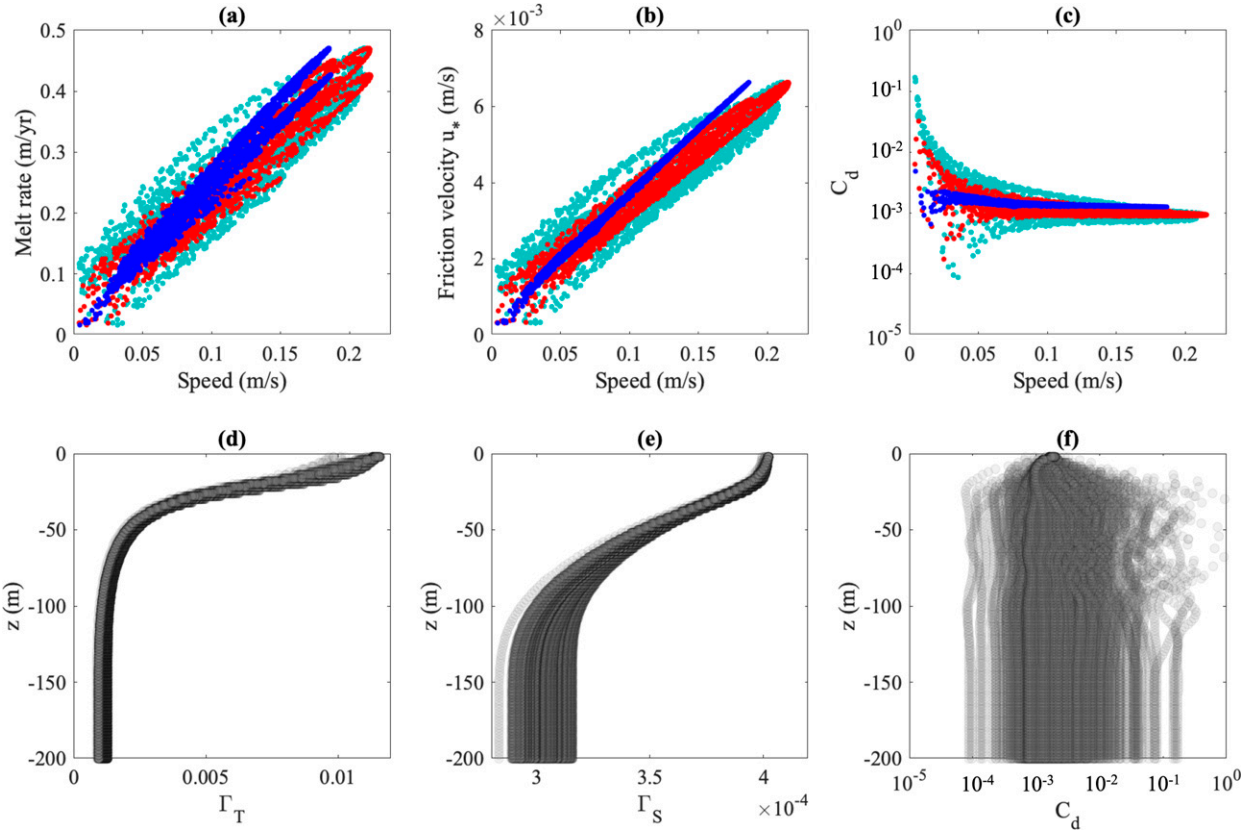

FIG. C2. The (a) melt rate, (b) friction velocity, and (c) drag coefficient against speed for a simulation with no slope. The transfer coefficients for (d) heat and (e) salt, and (f) the drag coefficient with depth for a simulation with no slope. The current speed and melt rate were averaged in the slope-parallel directions across the domain. The results are shown for days 70–100 of the simulation only. In (a)–(c) the symbol color corresponds to the depth at which C_d and the current speed were calculated (blue = 2.5-m depth, red = 13.5-m depth, and cyan = far field at 190-m depth). In (c) and (f) the drag coefficient was calculated using friction velocity at the ice base [Eq. (7)].

significantly. Finally, the melt rate is also compared between the resolved and near-wall model simulations.

Figure B1 shows the resolved LES (closed symbols) compared with the near-wall model LES (open symbols). The values of $T(z)$, $S(z)$, and $U(z)$ were taken at depth $z = -2$ m (the domain depth) for the output shown in Fig. B1. The model output could then also be compared with the Monin–Obukhov scaling, shown as the red lines in Fig. B1 [where Eqs. (B4) were calculated for $z = -2$ m rather than z_g]. The Monin–Obukhov scaling remains dependent on u_* and so there are two red lines on Figs. B1a–c. The Fig. B1d panel shows the thermal driving varying with melt rate, with the lines showing a theoretical limit on the melt rate for a "passive scalar" case where the gravity is turned off [more detail on the resolved LES in Vreugdenhil and Taylor (2019)].

Overall Fig. B1 shows that the near-wall model performs well when the flow is turbulent (large L^+) and melt rate and thermal driving are weak. This is demonstrated by consistency between the heat, salt, and momentum flux coefficients, along with the melt rate. When the thermal driving becomes strong the near-wall model salt transfer coefficient in particular begins to deviate from the resolved LES (Fig. B1b). This deviation is also where the resolved LES diverges from the Monin–Obukhov scaling, whereas the near-wall model values remain consistent with the Monin–Obukhov scaling. The latter result is perhaps unsurprising as the near-wall model is based on the Monin–Obukhov scaling.

For the ocean boundary layer beneath Larsen C Ice Shelf, Fig. B2 shows the evolution of the Obukhov length scale L^+ for the large domain near-wall model LES. For a large portion of the spring–neap tidal cycle $L^+ > 10^3$, especially in the time interval that was of most interest (day 70 onward). It was only for $L^+ < 10^3$ that there was significant departure for both Γ_T and Γ_S (Fig. B1). In the near-wall model LES, $L^+ < 10^3$ when the tidal forcing was weakest and friction velocity smallest. These intervals are relatively short and, as both melt rate and friction velocity were small here, we assume that the transfer coefficient departure did not significantly influence the overall flow.

APPENDIX C

Simulation Without the Slope and Plume

An additional large domain simulation was conducted with exactly the same set up as the original sloped simulation

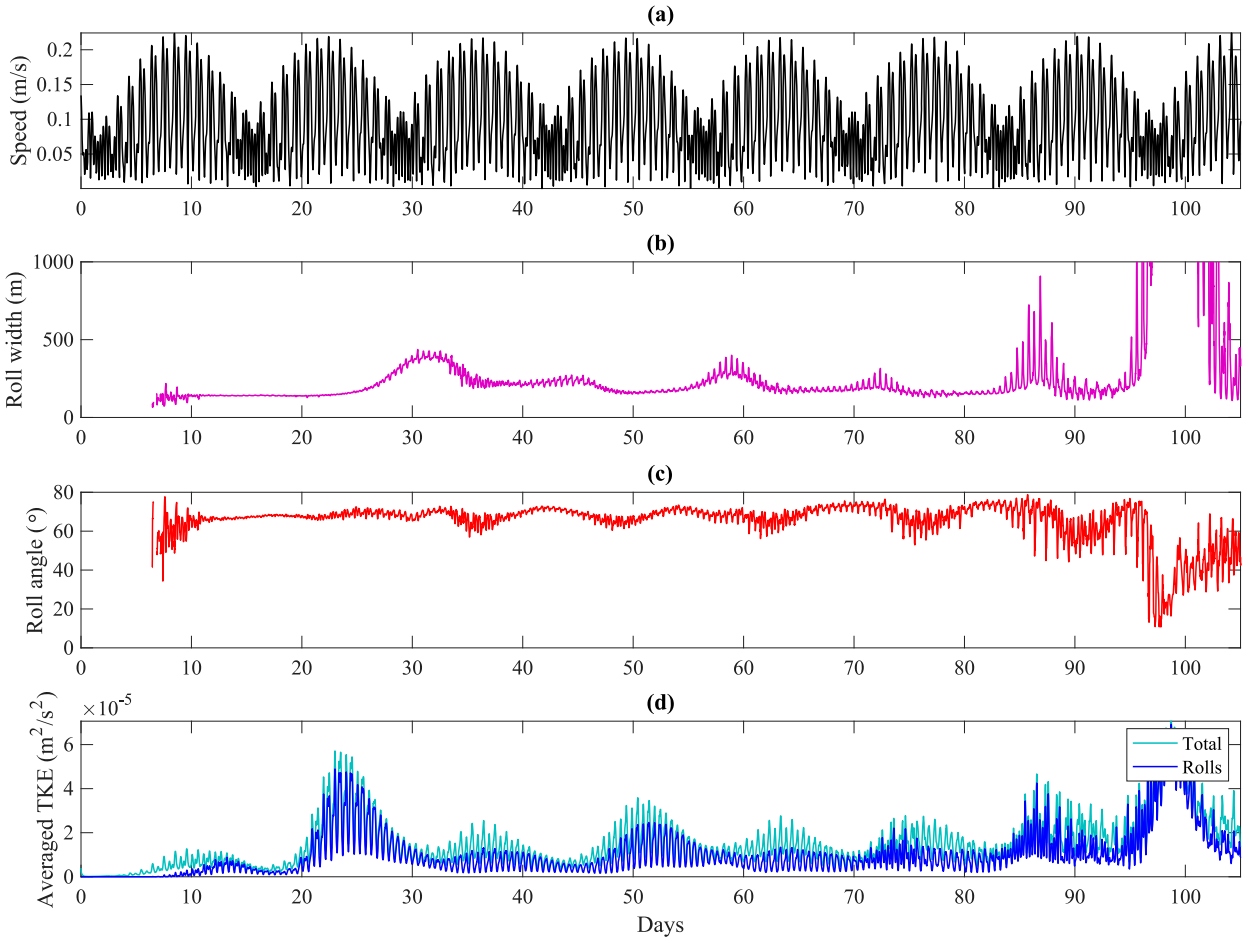

FIG. C3. The evolution of the Ekman rolls at depth $z = -20$ m for a simulation with no slope. (a) Mean current speed of the flow at $z = -20$ m, (b) roll width, (c) roll angle, and (d) averaged turbulent kinetic energy TKE. The TKE has been averaged across the slope-parallel slice at $z = -20$ m for each time step. The total of this average TKE is shown, along with the portion associated with the Ekman rolls. The Ekman roll portion of TKE was calculated using the chosen cutoff in wavenumber space (cut off value of TKE = 3×10^{-9} m^2 s^{-2} for the large domain grid resolution).

(outlined in section 2) but with no basal slope. The simulation was initialized in the same manner and run for over 100 days. There was almost no change in most of the flow properties examined here, with a couple of key exceptions outlined below.

The evolution of the slope-parallel velocity profiles is shown in Fig. C1. The Ekman layer was set up almost immediately (within the first 12-h period) but continued to change over time as the tides varied direction. The slow deepening of the mixed layer region is also shown in the velocity profiles. The simulations with and without the basal slope showed flow that was quite similar, but the sloped case showed more across-slope movement as there was a buoyant meltwater plume (Fig. C1). The buoyant plume was diverted to primarily across slope movement due to geostrophy (Jenkins 2016).

The bulk properties of the stratification evolved in a very similar manner regardless of the basal slope with minor influences on the bulk melt rate and friction velocities. One key difference appeared when comparing the far-field speed to the instantaneous melt rate and drag coefficient (Fig. C2). There is noticeably less skewness in the histogram of C_d values at a given speed (cyan lines) compared to the sloped simulation (Fig. 5c). This is consistent with a weak meltwater plume being present in the upper water column that has some distinct movement which is separate from the tidal forcing movement in the far field. The transfer coefficients Γ_T, Γ_S remain largely unchanged.

The other main difference was the evolution of the Ekman rolls (Fig. C3). The rolls formed in the same manner as the sloped simulation, including the same angle and about 200 m wide. Unlike the sloped simulation, the roll width in the flat ice case remained at about 200 m until the end of the simulation, where the signal became weak compared to other flow turbulence. The cutoff TKE then anomalously picked the domain size as the dominant mode—this is an artifact of the method for averaging TKE spectra if the overall signal becomes too weak. The roll contribution

to the total TKE was a similar contribution to the sloped case. The lack of a meltwater plume may be the reason that the roll width remains close to 200 m in the simulation with a flat ice base. We note that the mixed layer depth appeared to continue evolving in depth with time, similar to the sloped case, so this does not explain the limiting roll depth of 200 m.

REFERENCES

Abkar, M., and P. Moin, 2017: Large-eddy simulation of thermally stratified atmospheric boundary-layer flow using a minimum dissipation model. *Bound.-Layer Meteor.*, **165**, 405–419, https://doi.org/10.1007/s10546-017-0288-4.

Arzeno, I. B., R. C. Beardsley, R. Limeburner, B. Owens, L. Padman, S. R. Springer, C. L. Stewart, and M. J. Williams, 2014: Ocean variability contributing to basal melt rate near the ice front of Ross Ice Shelf, Antarctica. *J. Geophys. Res. Oceans*, **119**, 4214–4233, https://doi.org/10.1002/2014JC009792.

Bathmann, U., V. Smetacek, H. de Baar, E. Fahrbach, and G. Krause, 1994: The expeditions ANTARKTIS X/6-8 of the research vessel "POLARSTERN" in 1992/93. *Ber. Polarforsch.*, **135**, 236, https://doi.org/10.2312/BzP_0135_1994.

Begeman, C. B., and Coauthors, 2018: Ocean stratification and low melt rates at the Ross Ice Shelf grounding zone. *J. Geophys. Res. Oceans*, **123**, 7438–7452, https://doi.org/10.1029/2018JC013987.

Bradshaw, P., and G. P. Huang, 1995: The law of the wall in turbulent flow. *Proc. Roy. Soc. London*, **A451**, 165–188, https://doi.org/10.1098/rspa.1995.0122.

Brown, R. A., 1972: On the inflection point instability of a stratified Ekman boundary layer. *J. Atmos. Sci.*, **29**, 850–859, https://doi.org/10.1175/1520-0469(1972)029<0850:OTIPIO>2.0.CO;2.

Businger, J. A., J. C. Wyngaard, Y. Izumi, and E. F. Bradley, 1971: Flux-profile relationships in the atmospheric surface layer. *J. Atmos. Sci.*, **28**, 181–189, https://doi.org/10.1175/1520-0469(1971)028<0181:FPRITA>2.0.CO;2.

Darelius, E., I. Fer, and K. W. Nicholls, 2016: Observed vulnerability of Filchner-Ronne Ice Shelf to wind-driven inflow of warm deep water. *Nat. Commun.*, **7**, 12300, https://doi.org/10.1038/ncomms12300.

Davis, P. E. D., and K. W. Nicholls, 2019: Turbulence observations beneath Larsen C ice shelf, Antarctica. *J. Geophys. Res. Oceans*, **124**, 5529–5550, https://doi.org/10.1029/2019JC015164.

Deusebio, E., G. Brethouwer, P. Schlatter, and E. Lindborg, 2014: A numerical study of the unstratified and stratified Ekman layer. *J. Fluid Mech.*, **755**, 672–704, https://doi.org/10.1017/jfm.2014.318.

——, C. P. Caulfield, and J. R. Taylor, 2015: The intermittency boundary in stratified plane Couette flow. *J. Fluid Mech.*, **781**, 298–329, https://doi.org/10.1017/jfm.2015.497.

Dinniman, M. S., X. S. Asay-Davis, B. K. Galton-Fenzi, P. R. Holland, A. Jenkins, and R. Timmermann, 2016: Modeling ice shelf/ocean interaction in Antarctica: A review. *Oceanography*, **29**, 144–153, https://doi.org/10.5670/oceanog.2016.106.

Faller, A. J., and R. E. Kaylor, 1966: A numerical study of the instability of the laminar Ekman boundary layer. *J. Atmos. Sci.*, **23**, 466–480, https://doi.org/10.1175/1520-0469(1966)023<0466:ANSOTI>2.0.CO;2.

Foken, T., 2006: 50 years of the Monin–Obukhov similarity theory. *Bound.-Layer Meteor.*, **119**, 431–447, https://doi.org/10.1007/s10546-006-9048-6.

Fretwell, P., and Coauthors, 2013: Bedmap2: Improved ice bed, surface and thickness datasets for Antarctica. *Cryosphere*, **7**, 375–393, https://doi.org/10.5194/tc-7-375-2013.

Gayen, B., R. W. Griffiths, and R. C. Kerr, 2016: Simulation of convection at a vertical ice face dissolving into saline water. *J. Fluid Mech.*, **798**, 284–298, https://doi.org/10.1017/jfm.2016.315.

Hattermann, T., O. A. Nøst, J. M. Lilly, and L. H. Smedsrud, 2012: Two years of oceanic observations below the Fimbul Ice Shelf, Antarctica. *Geophys. Res. Lett.*, **39**, L12605, https://doi.org/10.1029/2012GL051012.

Hellmer, H. H., F. Kauker, R. Timmermann, J. Determann, and J. Rae, 2012: Twenty-first-century warming of a large Antarctic ice-shelf cavity by a redirected coastal current. *Nature*, **485**, 225–228, https://doi.org/10.1038/nature11064.

Holland, D. M., and A. Jenkins, 1999: Modeling thermodynamic ice–ocean interactions at the base of an ice shelf. *J. Phys. Oceanogr.*, **29**, 1787–1800, https://doi.org/10.1175/1520-0485(1999)029<1787:MTIOIA>2.0.CO;2.

Holland, P. R., T. J. Bracegirdle, P. Dutrieux, A. Jenkins, and E. J. Steig, 2019: West Antarctic ice loss influenced by internal climate variability and anthropogenic forcing. *Nat. Geosci.*, **12**, 718–724, https://doi.org/10.1038/s41561-019-0420-9.

Jenkins, A., 1991: A one-dimensional model of ice shelf-ocean interaction. *J. Geophys. Res.*, **96**, 20 671–20 677, https://doi.org/10.1029/91JC01842.

——, 2011: Convection-driven melting near the grounding lines of ice shelves and tidewater glaciers. *J. Phys. Oceanogr.*, **41**, 2279–2294, https://doi.org/10.1175/JPO-D-11-03.1.

——, 2016: A simple model of the ice shelf–ocean boundary layer and current. *J. Phys. Oceanogr.*, **46**, 1785–1803, https://doi.org/10.1175/JPO-D-15-0194.1.

——, 2021: Shear, stability, and mixing within the ice shelf–ocean boundary current. *J. Phys. Oceanogr.*, **51**, 2129–2148, https://doi.org/10.1175/JPO-D-20-0096.1.

——, K. W. Nicholls, and H. F. J. Corr, 2010: Observation and parameterization of ablation at the base of Ronne Ice Shelf, Antarctica. *J. Phys. Oceanogr.*, **40**, 2298–2312, https://doi.org/10.1175/2010JPO4317.1.

——, D. Shoosmith, P. Dutrieux, S. Jacobs, T. W. Kim, S. H. Lee, H. K. Ha, and S. Stammerjohn, 2018: West Antarctic Ice Sheet retreat in the Amundsen Sea driven by decadal oceanic variability. *Nat. Geosci.*, **11**, 733–738, https://doi.org/10.1038/s41561-018-0207-4.

Jiménez, J., 2004: Turbulent flows over rough walls. *Annu. Rev. Fluid Mech.*, **36**, 173–196, https://doi.org/10.1146/annurev.fluid.36.050802.122103.

Kader, B., and A. Yaglom, 1972: Heat and mass transfer laws for fully turbulent wall flows. *Int. J. Heat Mass Transf.*, **15**, 2329–2351, https://doi.org/10.1016/0017-9310(72)90131-7.

Kaimal, J., J. Wyngaard, D. Haugen, O. Coté, Y. Izumi, S. Caughey, and C. Readings, 1976: Turbulence structure in the convective boundary layer. *J. Atmos. Sci.*, **33**, 2152–2169, https://doi.org/10.1175/1520-0469(1976)033<2152:TSITCB>2.0.CO;2.

Keitzl, T., J. P. Mellado, and D. Notz, 2016: Reconciling estimates of the ratio of heat and salt fluxes at the ice-ocean interface. *J. Geophys. Res. Oceans*, **121**, 8419–8433, https://doi.org/10.1002/2016JC012018.

Kimura, S., K. W. Nicholls, and E. Venables, 2015: Estimation of ice shelf melt rate in the presence of a thermohaline staircase. *J. Phys. Oceanogr.*, **45**, 133–148, https://doi.org/10.1175/JPO-D-14-0106.1.

——, A. Jenkins, P. Dutrieux, A. Forryan, A. C. Naveira Garabato, and Y. Firing, 2016: Ocean mixing beneath Pine Island glacier ice shelf, West Antarctica. *J. Geophys. Res. Oceans*, **121**, 8496–8510, https://doi.org/10.1002/2016JC012149.

Lilly, D. K., 1966: On the instability of Ekman boundary flow. *J. Atmos. Sci.*, **23**, 481–494, https://doi.org/10.1175/1520-0469(1966)023<0481:OTIOEB>2.0.CO;2.

Lilly, J. M., 2017: Element analysis: A wavelet-based method for analysing time-localized events in noisy time series. *Proc. Roy. Soc.*, **A473**, 20160776, http://doi.org/10.1098/rspa.2016.0776.

Malyarenko, A., A. J. Wells, P. J. Langhorne, N. J. Robinson, M. J. Williams, and K. W. Nicholls, 2020: A synthesis of thermodynamic ablation at ice-ocean interfaces from theory, observations and models. *Ocean Model.*, **154**, 101692, https://doi.org/10.1016/j.ocemod.2020.101692.

Martin, S., and P. Kauffman, 1977: An experimental and theoretical study of the turbulent and laminar convection generated under a horizontal ice sheet floating on warm salty water. *J. Phys. Oceanogr.*, **7**, 272–283, https://doi.org/10.1175/1520-0485(1977)007<0272:AEATSO>2.0.CO;2.

McConnochie, C. D., and R. C. Kerr, 2016: The effect of a salinity gradient on the dissolution of a vertical ice face. *J. Fluid Mech.*, **791**, 589–607, https://doi.org/10.1017/jfm.2016.62.

——, and ——, 2018: Dissolution of a sloping solid surface by turbulent compositional convection. *J. Fluid Mech.*, **846**, 563–577, https://doi.org/10.1017/jfm.2018.282.

McDougall, T. J., and P. M. Barker, 2011: Getting started with TEOS-10 and the Gibbs Seawater (GSW) Oceanographic Toolbox. SCOR/IAPSO WG127, 28 pp., http://www.teos-10.org/pubs/Getting_Started.pdf.

McPhee, M. G., G. A. Maykut, and J. H. Morison, 1987: Dynamics and thermodynamics of the ice/upper ocean system in the marginal ice zone of the Greenland Sea. *J. Geophys. Res.*, **92**, 7017–7031, https://doi.org/10.1029/JC092iC07p07017.

Middleton, L., C. A. Vreugdenhil, P. R. Holland, and J. R. Taylor, 2021: Numerical simulations of melt-driven double-diffusive fluxes in a turbulent boundary layer beneath an ice shelf. *J. Phys. Oceanogr.*, **51**, 403–418, https://doi.org/10.1175/JPO-D-20-0114.1.

Mkhinini, N., T. Dubos, and P. Drobinski, 2013: Secondary instability of the stably stratified Ekman layer. *J. Fluid Mech.*, **728**, 29–57, https://doi.org/10.1017/jfm.2013.250.

Moeng, C.-H., 1984: A large-eddy-simulation model for the study of planetary boundary-layer turbulence. *J. Atmos. Sci.*, **41**, 2052–2062, https://doi.org/10.1175/1520-0469(1984)041<2052:ALESMF>2.0.CO;2.

Mondal, M., B. Gayen, R. W. Griffiths, and R. C. Kerr, 2019: Ablation of sloping ice faces into polar seawater. *J. Fluid Mech.*, **863**, 545–571, https://doi.org/10.1017/jfm.2018.970.

Nicholls, K. W., C. Pudsey, and P. Morris, 2004: Summertime water masses off the northern Larsen C Ice Shelf, Antarctica. *Geophys. Res. Lett.*, **31**, L09309, https://doi.org/10.1029/2004GL019924.

——, K. Makinson, and E. Venables, 2012: Ocean circulation beneath Larsen C Ice Shelf, Antarctica from in situ observations. *Geophys. Res. Lett.*, **39**, L19608, https://doi.org/10.1029/2012GL053187.

Orszag, S. A., 1971: Numerical simulation of incompressible flows within simple boundaries. 1. Galerkin (spectral) representation. *Stud. Appl. Math.*, **50**, 293–327, https://doi.org/10.1002/sapm1971504293.

Paolo, F. S., H. A. Fricker, and L. Padman, 2015: Volume loss from Antarctic ice shelves is accelerating. *Science*, **348**, 327–331, https://doi.org/10.1126/science.aaa0940.

Piomelli, U., J. Ferziger, P. Moin, and J. Kim, 1989: New approximate boundary conditions for large eddy simulations of wall-bounded flows. *Phys. Fluids A*, **1**, 1061–1068, https://doi.org/10.1063/1.857397.

Pope, S. B., 2000: *Turbulent Flows.* Cambridge University Press, 802 pp.

Pritchard, H., S. R. Ligtenberg, H. A. Fricker, D. G. Vaughan, M. R. van den Broeke, and L. Padman, 2012: Antarctic ice-sheet loss driven by basal melting of ice shelves. *Nature*, **484**, 502–505, https://doi.org/10.1038/nature10968.

Rosevear, M. G., B. Gayen, and B. K. Galton-Fenzi, 2021: The role of double-diffusive convection in basal melting of Antarctic ice shelves. *Proc. Natl. Acad. Sci. USA*, **118**, e2007541118, https://doi.org/10.1073/pnas.2007541118.

Rozema, W., H. J. Bae, P. Moin, and R. Verstappen, 2015: Minimum-dissipation models for large-eddy simulation. *Phys. Fluids*, **27**, 085107, https://doi.org/10.1063/1.4928700.

Schlichting, H., and K. Gersten, 2003: *Boundary-Layer Theory.* Springer, 800 pp.

Schoof, C., 2007: Ice sheet grounding line dynamics: Steady states, stability, and hysteresis. *J. Geophys. Res.*, **112**, F03S28, https://doi.org/10.1029/2006JF000664.

Shepherd, A., D. Wingham, and E. Rignot, 2004: Warm ocean is eroding West Antarctic ice sheet. *Geophys. Res. Lett.*, **31**, L23402, https://doi.org/10.1029/2004GL021106.

Stanton, T. P., and Coauthors, 2013: Channelized ice melting in the ocean boundary layer beneath Pine Island Glacier. *Science*, **341**, 1236–1239, https://doi.org/10.1126/science.1239373.

Taylor, J. R., 2008: Numerical simulations of the stratified oceanic bottom boundary layer. Ph.D. thesis, University of California, San Diego, 230 pp., https://escholarship.org/uc/item/5s30n2ts.

Verstappen, R., 2016: How much eddy dissipation is needed to counterbalance the nonlinear production of small, unresolved scales in a large-eddy simulation of turbulence? *Comput. Fluids*, **176**, 276–284, https://doi.org/10.1016/j.compfluid.2016.12.016.

Vreugdenhil, C. A., and J. R. Taylor, 2018: Large-eddy simulations of stratified plane Couette flow using the anisotropic minimum-dissipation model. *Phys. Fluids*, **30**, 085104, https://doi.org/10.1063/1.5037039.

——, and ——, 2019: Stratification effects in the turbulent boundary layer beneath a melting ice shelf: Insights from resolved large-eddy simulations. *J. Phys. Oceanogr.*, **49**, 1905–1925, https://doi.org/10.1175/JPO-D-18-0252.1.

Wyngaard, J. C., 2010: *Turbulence in the Atmosphere.* Cambridge University Press, 393 pp.

Zhou, Q., J. R. Taylor, and C. P. Caulfield, 2017: Self-similar mixing in stratified plane Couette flow for varying Prandtl number. *J. Fluid Mech.*, **820**, 86–120, https://doi.org/10.1017/jfm.2017.200.